

HST IMAGING OF CFRS and LDSS galaxies

— I: Morphological Properties*

Jarle Brinchmann¹, Roberto Abraham¹, David Schade², Laurence Tresse¹, Richard S. Ellis¹,
 Simon Lilly^{1,3}, Olivier Le Fèvre^{4,6}, Karl Glazebrook⁵, François Hammer⁶, Matthew Colless⁷,
 David Crampton², Tom Broadhurst⁸

ABSTRACT

We analyse Hubble Space Telescope images of a complete sample of 341 galaxies drawn from both the Canada France and Autofib/Low Dispersion Survey Spectrograph ground-based redshift surveys. In this, the first paper in the series, each galaxy has been morphologically classified according to a scheme similar to that developed for the Medium Deep Survey. We discuss the reproducibility of these classifications and quantify possible biases that may arise from various redshift-dependent effects. We then discuss automated classifications of the sample and conclude, from several tests, that we can expect an apparent migration with redshift to later Hubble types that corresponds to a misclassification in our adopted machine classification system of $\sim 24\% \pm 11$ of the true “spirals” as “peculiars” at a redshift $z \simeq 0.9$. After allowing for such biases, the redshift distribution for normal spirals, together with their luminosity function derived as a function of redshift, indicates approximately 1 magnitude of luminosity evolution in B_{AB} by $z \simeq 1$. The elliptical sample is too small for precise evolutionary constraints. However, we find a substantial increase in the proportion of galaxies with irregular morphology at large redshift from $9\% \pm 3\%$ for $0.3 \leq z \leq 0.5$ to $32\% \pm 12\%$ for $0.7 \leq z \leq 0.9$. These galaxies also appear to be the dominant cause of the rapid rise with redshift in the blue luminosity density identified in the redshift surveys. Although galaxies with irregular morphology may well comprise a mixture of

¹Institute of Astronomy, Madingley Road, Cambridge CB3 0HA

²Dominion Astrophysical Observatory, Victoria, Canada

³Department of Astronomy, University of Toronto, Toronto, Canada

⁴Laboratoire d’Astronomie Spatiale, Traverse du Siphon, B.P.8, 13376 Marseille Cedex 12, France

⁵Anglo-Australian Observatory. Siding Spring Observatory, Coonabarabran, NSW 2357, Australia

⁶Observatoire de Paris, Section de Meudon, DAEC, 92195 Meudon Principal Cedex, France

⁷Mt. Stromlo and Siding Spring Observatories, Australian National University, Weston Creek, ACT 2611, Australia

⁸Astronomy Department, University of California, Berkeley, CA 94720, US

*Based on observations with the NASA/ESA *Hubble Space Telescope* obtained at the Space Telescope Science Institute, which is operated by the Association of Universities for Research in Astronomy, Inc., under NASA contract NAS 5-26555

different physical systems and might not correspond to present day irregulars, it is clear that the apparently declining abundance and luminosities of our distant “irregulars” holds an important key to understanding recent evolution in the star formation history of normal galaxies.

1. Introduction

The refurbished Hubble Space Telescope (HST) offers the exciting prospect of addressing the morphological evolution of galaxies directly from systematic studies of galaxies imaged at various redshifts. The angular resolution of the Wide Field Planetary Camera 2 (WFPC-2) is 0.1 arcsec which corresponds to a physical scale of less than 2 kpc at all redshifts in most popular cosmological world models (we have assumed $H_0 = 50 \text{ km s}^{-1} \text{ Mpc}^{-1}$ here and will adopt this value and $q_0 = 0.5$ in the rest of the paper).

Considerable progress in understanding the morphological mixture of the faint galaxy population has already been achieved through the Medium Deep Survey (Griffiths et al. 1994; Driver et al. 1995a), an extensive imaging programme using WFPC-2 in parallel mode. Counts of galaxies classed by visual morphology (Glazebrook et al. 1995a; Driver et al. 1995a) and by other means (Abraham et al. 1996b; Odewahn et al. 1996) have been compared with model predictions and an apparent excess of ‘irregular/peculiar/merger’ galaxies is noted when compared to models based on no evolution. Deeper HST images of smaller areas have been taken using WFPC-2 in primary mode. Driver et al. 1995b have analysed a single deeper pointed exposure of 5.7 hours confirming and extending the MDS analysis to $I=24.5$. Abraham et al (1996b) have likewise categorised galaxies in the Hubble Deep Field to $I=25$. Given the magnitude limits over which these changes are seen, the above studies point to fairly recent changes in the morphological characteristics of the galaxy population.

Similar progress has been made from large systematic ground-based spectroscopic surveys which serve to delineate the field galaxy luminosity function (LF) and its evolution out to redshifts $z \simeq 1$. The I -selected Canada France Redshift Survey (CFRS, Lilly et al. 1995a; Le Fèvre et al. 1995 and references therein) comprises a complete spectroscopic sample of 591 galaxies in the magnitude range $17.5 \leq I_{AB} \leq 22.5$ with determined redshifts. The rest-frame B_{AB} -band LF has been determined for various redshifts and colour-selected components of the population. Strong evolution with redshift is found in the luminosity function of the bluer galaxies. These trends are supported by those from the less deep, but also extensive, Autofib/Low Dispersion Survey Spectrograph (hereafter LDSS) redshift survey (Ellis et al. 1996 and references therein). This survey is b_J -selected and spans a wide apparent magnitude range ($11.5 < b_J < 24$) enabling the *shape* of the star-forming component of the LF to be monitored to $z=0.75$. Strong evolution is seen in terms of the space density and luminosity of galaxies with intense star formation categorised via their [OII] emission. Using the same data Heyl et al (1997) showed that it is the late *spectral* types that dominate the evolution out to $z \simeq 0.5$. Both surveys are consistent with a large decline

in the luminosity density of star forming galaxies since a redshift of 1 (Lilly et al. 1996; Ellis et al. 1996).

The HST imaging and ground-based spectroscopic surveys present different but complementary views of the evolving galaxy population since $z \simeq 1$. Indeed, it is tempting to connect the rapid increase with look-back time in the proportion of galaxies in the irregular/peculiar/merger category with the strong evolution seen in the star-forming blue sources in the redshift surveys. However, until recently, there has been surprisingly little overlap between the wealth of HST data and the ground-based redshift surveys, largely because of the mismatch in field size between WFPC-2 and ground-based multi-object spectrographs.

In this series of papers we plan to remedy this deficiency via a HST imaging programme of 341 galaxies targetted in either the CFRS or LDSS surveys. The goals of the study are to employ techniques developed in the analyses of both the HST and ground-based datasets to physically understand the origin of the remarkably recent evolutionary trends identified in the independent datasets.

This paper is concerned with describing the survey parameters and selection criteria and the techniques used to analyse the HST data. Further details of the ground-based spectroscopic datasets can be found in the CFRS and LDSS articles (Crampton et al. 1995; Ellis et al. 1996). By bringing together HST and redshift data for a large complete sample of distant galaxies, we address in this paper the question of whether the rapid evolution in the morphologically peculiar population can be identified with the star-forming blue sources in the redshift surveys. As shown below, the correspondence is convincing, as originally conjectured by the MDS studies.

A plan of the paper follows. In Section 2 we discuss the basic features of the LDSS and CFRS redshift surveys. As the photometric systems and the treatment of k-corrections differ between the two surveys, we compare and align these prior to further analysis. The HST imaging data is introduced in Section 3 and both visual and automated morphological classifications are presented. A major question is the extent to which the apparent morphological type recognised in the HST data is affected by redshift-dependent biases. Through simulations based on local multicolour imaging data, we address this point in detail in Section 4 and obtain statistical correction factors which are applied in the subsequent analyses. Section 5 presents the redshift distributions and luminosity functions for three broad morphological classes. We also discuss the associated blue luminosity density for each type as a function of redshift and interpret this in the context of simple models put forward to explain the evolutionary trends found in the redshift survey data. Our main conclusions are summarised in Section 6.

Later papers in the series use structural parameters for each HST image to discuss the physical processes that drive this evolution. Lilly et al. (1997) (Paper II) examines the surface brightness characteristics of the largest disk galaxies in order to constrain the extent to which evolution of massive galaxies may be important. Schade et al. (1997) (Paper III) addresses the question of evolution in the number density and photometric properties of the spheroidal

population. Papers II and III both concentrate on quantitative morphological measures for the galaxies, extending and improving the analysis in Schade et al. (1995). Le Fèvre et al. (1997) (Paper IV) perform quantitative measures of clustering on small physical scales and use this to study the rate of merging as a function of redshift.

2. Survey Description

Upon completion of the CFRS and LDSS redshift surveys both CFRS and LDSS teams independently sought HST WFPC–2 time in Cycle 4. Early results from these programmes have been described by Schade et al. (1995) and Ellis (1995). From 1994, both teams agreed to merge their efforts and further allocations of HST time to the combined team were made in Cycles 5 and 6.

In Cycle 4, prior to the merged effort, the strategy adopted by two teams was somewhat different. Although both teams sought F814W imaging for morphological classifications, the CFRS team chose to supplement these images with ones in F450W whereas the LDSS team explored the visibility of their b_J -selected samples in F336W and F218W. Only in Cycles 5 and 6 did a common strategy emerge based on F814W images augmented by F450W images for a subset of the targets.

It is important to recognise that the ground-based strategies adopted by the CFRS and LDSS survey teams differed in several respects. Foremost the CFRS survey is I -selected whereas the LDSS survey is b_J -selected. The strong differential effects of k-correction with galaxy type mean that, although the LDSS survey is shallower, it is more sensitive to the presence of star-forming galaxies that apparently dominate the evolutionary trends. By contrast, the CFRS survey is less affected by k-correction effects overall and probes to higher redshift. Both teams chose to present their data in terms of rest-frame blue magnitudes although CFRS presented LFs on a photometric scale based on B(AB) whereas the LDSS team did so in b_J . The transformation between these two magnitude scales is studied below.

Table 1 summarises the HST survey data obtained for this analysis. The total dataset consists of 341 objects drawn from 25 WFPC–2 HST frames. 6 fields are drawn from the contiguous ‘Groth strip’ (Groth et al. 1994) imaged by WFPC–2 for which supplementary spectroscopy of 59 objects was obtained to a magnitude limit identical to that adopted for the main CFRS survey using LDSS-2 on the 4.2m William Herschel Telescope. Galaxies have only been included in the final catalogue if they have been spectroscopically targeted in either the CFRS, LDSS or Groth strip surveys. 37 objects were excised as their HST images are partially or completely obscured by edges of the WFPC chips or cosmetic defects precluding accurate morphological analysis. The catalogue contains 7 objects from the Autofib fibre survey (Ellis et al. 1996) as well as 22 LDSS-1 (Colless et al. 1993 and references therein) objects. The spectroscopic completeness for these objects is only 62%, and they will not be discussed further in the present paper since little is gained in terms of numbers; we will instead concentrate on galaxies from the CFRS and LDSS-2

(Glazebrook et al. 1995b) surveys. The absolute magnitude – redshift distributions of the objects from the CFRS and LDSS-2 samples and the sub-samples for which HST data is available are compared in Figure 1. It can be seen that the two surveys span different regions in this parameter space. The CFRS survey is particularly useful in probing all classes of luminous galaxies in the interval $0.5 < z < 1$, whereas the LDSS survey is effective in probing less luminous star-forming galaxies in the interval $0.2 < z < 0.7$. The complete catalogue of galaxies comprising the HST survey is given together with detailed comments in Table 2.

All observed fields were imaged through the F814W filter which ensures that a self-consistent and uniform photometric scale can be provided across both the CFRS and LDSS galaxies. Only the CFRS survey galaxies currently have reliable ground-based I_{AB} photometry. To achieve a uniform photometric scale, the raw HST images were processed using the standard STScI pipeline, and photometry in the F814W system was performed using the Iraf `apphot` package with $3''$ diameter apertures. The zero-point calibration was taken from Holtzman et al (1995). The colour transformation between I_{AB} and I_{F814} was calculated for the CFRS galaxies by interpolating within the observed $V - I$ colours according to a set of spectral energy distributions (SEDs); good agreement with the ground based magnitudes was found.

As it was not possible to image *all* the ground-based fields in both surveys within the HST time allocated, the LDSS group initially selected their fields on the basis of maximising the fraction of targets for which redshifts had been secured, whereas the CFRS group originally imaged fields to maximise the fraction of high redshift objects. After the two groups joined forces, it was agreed that no particular criterion should be used to select the remaining fields. We have, retrospectively, verified that the earlier selection criteria have not unduly weighted the HST survey to an unrepresentative sample of galaxies.

The completeness in the original ground-based surveys varies from field to field primarily because of the vagaries of weather at the time of the original observations. The completeness statistics are given in Table 3 for the subset of galaxies in the survey that were either in the CFRS or LDSS-2 redshift surveys. The completeness is only marginally higher than that appropriate for the parent survey.

Figure 2 shows the redshift distribution separately for the CFRS and LDSS-2 objects in the HST survey. Clearly a greater fraction of the CFRS galaxies have been selected for study with HST than is the case for the LDSS survey. The median redshift for the HST-selected CFRS objects, $\langle z \rangle = 0.61$, can be compared with $\langle z \rangle = 0.56$ for the entire CFRS ground-based survey. For the LDSS-2 objects the difference is similarly small — $\langle z \rangle = 0.46$ in the ground-based survey compared with $\langle z \rangle = 0.43$ in the HST imaged subset.

Clearly it is important to construct a uniform absolute magnitude scale across the two surveys. This is an important problem not only because of observational differences in the photometric selection criteria used by the two groups but also because of procedural differences used in estimating the k -corrections. To check the photometric differences, we transformed the

LDSS-2 b_J photometry to the B_{AB} system used by the CFRS. The required $b_J - B_{AB}$ colour was found by using the LDSS-2 $b_J - r_F$ to define an SED from which the colour offset was located by interpolation. A histogram of the offsets obtained in this manner is shown in the top panel of Figure 3, where it is seen that the offset and scatter are both quite small compared to the bin widths we will use in discussing evolutionary trends e.g. in the LF.

To investigate systematical differences in the k -corrections used between the two groups, we compared the k -corrections derived for a subset of CFRS galaxies using their set of SEDs located via the $V - I$ colour with those defined similarly based on the LDSS-2 set of SEDs. The agreement is again surprisingly good indicating a dispersion of only $0^m 1$ and no systematic offset of significance (see middle panel Figure 3).

There is one further procedural difference concerning the surveys. In the case of the CFRS survey, the absolute magnitudes are derived from isophotal I_{AB} magnitudes whereas the LDSS-2 group used corrected aperture magnitudes. To determine the offsets involved, we note that the $3''$ aperture HST magnitudes for the faint CFRS objects agree well with their ground based isophotal magnitudes. We therefore measured $3''$ aperture magnitudes for the LDSS-2 objects on the HST images and calculated absolute magnitudes from these which were then compared with the published LDSS-2 absolute magnitudes. This comparison is shown in the bottom panel of Figure 3 and reveals no significant shift with a dispersion of only $0^m 2$, enabling us to conclude that the LDSS-2 corrected aperture magnitudes are closely equivalent to the CFRS I_{AB} isophotal magnitudes. The photometric systems can thus be aligned by adding the colour term to the LDSS absolute magnitudes.

In conclusion, within the typical photometric error of $0^m 2$, there is no evidence of a serious systematic shift between the two absolute magnitude scales. For consistency, all absolute magnitudes for galaxies drawn from *both* surveys were calculated with the same program using I_{AB} isophotal magnitudes for CFRS objects and $3''$ I aperture magnitudes from HST for the LDSS objects. In the subsequent analyses, virtually identical results are obtained when the published absolute magnitudes are used.

3. Classifications

To physically interpret the evolution of the galaxy LF as delineated by the original ground-based redshift surveys, both the CFRS and LDSS analyses sub-divided the samples on the basis of spectroscopic and photometric classes. CFRS analyses of the LF based on rest-frame color found luminosity evolution to be stronger for galaxies bluer than a Sbc. LDSS samples selected according to the rest-frame equivalent width of the [O II] 3727 line found that the evolutionary trends arose almost exclusively from galaxies with strong emission-lines.

The availability of the HST data for 341 galaxies allows us to investigate these changes in more detail. Ideally galaxies should be classified according to a label which is not modified by

any of the physical processes responsible for the evolution. Part of the difficulty with colour and emission line strength is that populations defined according to these criteria may well be transient, and thus detailed comparisons of luminosities and volume densities at various redshifts will be confused.

Although the same criticisms can no doubt be applied to galaxy morphology (White 1996), the morphologically-dependent number magnitude counts derived from the Medium Deep Survey and Hubble Deep Field (Glazebrook et al. 1995a; Driver et al. 1995a; Abraham et al. 1996b) raise important questions concerning the apparent rapid evolution of the irregular/peculiar/merger galaxies in comparison with the slower trends noted for the spheroidal and regular spiral classes. How do these classifications map onto the redshift survey data plane? In this section we discuss the various ways in which we have classified the galaxy morphologies taking care to note these uncertainties and systematic changes that may occur because our survey samples galaxies over a large range of redshifts.

3.1. Visual Classifications

The first technique we used to investigate the morphological characteristics of our sample follows the visual approach adopted by the Medium Deep Survey team. Following the precepts discussed by Glazebrook et al. (1995b), three of us (RSE, SJL, OLF) have classified all the galaxies by eye according to a scheme illustrated in Figure 4. The scheme we have adopted here differs slightly from that utilised by the MDS team in that we decided to separate compact objects with faint extensions (so-called “tadpoles”) from the irregular/merger/peculiar and compact objects. This was done for objects for which classifications were either compact or peculiar and where no consensus could be reached.

An intercomparison of the eyeball classifications between the 3 observers is shown in Figure 5 and indicates a scatter of around 1.2 classes. This is similar to the scatter found by the MDS team (Abraham et al. 1996a) at the same magnitude limit. The individual classifications were then merged by taking the median value of the different classifiers. The final number of objects in various classes is also indicated in Figure 4. The resulting $M_B - z$ diagram is shown in Figure 6 with the fractional redshift distributions of the various morphological classes inlaid.

In order to determine whether the morphological mixture is robustly estimated, we can compare the morphologically segregated $N(m)$ for our sample with that for the MDS survey (Abraham et al. 1996b; Glazebrook et al. 1995a). Since the MDS survey is I -selected, we can only compare it with that subset of our galaxies drawn from the CFRS survey. As the CFRS survey did not target all objects lying between the photometric limits, we must correct for those objects that are in the HST field within the magnitude limits which were not targetted spectroscopically. We have done this by multiplying the counts in each field with the ratio of photometrically to spectroscopically observed objects for each HST frame, taken from the CFRS survey. The resulting

counts are shown in Figure 7. It can be seen that there is an apparent lack of bright irregular galaxies. This is in part because the bright irregulars by coincidence happen to be in fields with high completeness. By assigning the bright irregulars to random fields we find the difference between our irregular counts and the MDS counts is generally less than 2σ and we do not consider this as a potential problem, as we will see the abundance of low redshift irregulars is almost exactly as expected from the local luminosity function (see Section 5.1). We find an integrated count from $I_{AB} = 17.5$ to $I_{AB} = 22.5$ from our survey of 394 whereas that expected from the MDS survey is 409, i.e. in close agreement. The field to field variation of the morphological composition is also satisfactorily constant to within the uncertainties.

3.2. Automated Classifications

A major difficulty with visual classifiers is their subjective nature (Naim et al. 1995). Accordingly, as an objective route forward, we have also performed machine-based classifications using the procedures adopted by Abraham et al. (1994,1996b). The technique is based on measurements of a central concentration index, C , and a rotational asymmetry factor, A . The first of these parameters tracks the bulge-to-disk ratio, while the second traces the degree of irregularity. At low redshift, the positions of galaxies on the $\log(A)$ vs $\log(C)$ plane can be used to distinguish between early-type systems, spirals earlier than type Sd, late-type spirals and irregulars/peculiars/mergers. As will be shown below, at higher redshifts these classes can also be distinguished in principle using a $A - C$ diagram. However, uncertainties arise because galaxies of a given type may move into a region of the $A - C$ plane occupied by a different class because of redshift-dependent effects. These biases must be carefully studied before quantitative comparisons can be made over a range in redshift. We defer a discussion of these studies until the next section.

The starting point for measuring the two parameters is a “segmented” galaxy image, constructed by isolating those pixels that lie above a surface brightness threshold $N\sigma$ above the sky brightness, where σ is the sky variance and N is a constant, typically 1.5. For the present work (see discussion below and in Appendix A), we have chosen σ so the measurements go to a uniform limiting surface brightness. The C parameter represents the ratio of light within an inner and outer elliptical aperture determined from the sky-subtracted, intensity-weighted, second order moment of the resulting image. The major and minor axes of the outer aperture are normalized so that the total area within the ellipse is the isophotal area of the galaxy. The inner aperture is defined by scaling these axes down by a linear factor of three.

Whereas this definition of central concentration is adequate for local galaxies, the value determined unfortunately depends on redshift since the threshold is defined relative to the sky. Thus less of the galaxy is sampled at high redshift because of cosmological dimming. Measuring C to a fixed rest-frame surface brightness isophote is not really practical so it is necessary to consider how to correct C for this effect. A procedure to do this is discussed in Appendix A, and in the rest of the paper all C values have been corrected using the minimal correction defined in

equation (A3).

The rotational asymmetry parameter A is defined via:

$$A = \frac{\sum_{ij} |I_{ij} - I_{ij}^R|}{\sum_{ij} I_{ij}} - k_A. \quad (1)$$

where I_{ij} is the intensity in pixel (i, j) , and I_{ij}^R is the corresponding intensity after image rotation by 180° about the centroid of the segmented galaxy image. The k_A term in equation (1) is a small correction accounting for signal introduced into A by noise in the sky background; k_A is determined by measuring the asymmetry within a rotated and self-subtracted region of sky equal in area to that of the galaxy being analysed.

The measurement of these parameters is only practical for that subset of galaxy images with more than 64 contiguous WFPC-2 pixels above the surface brightness threshold (see also the discussion in Abraham et al. 1994). 25 galaxies are too compact for reliable classification via this approach. For these objects, only the visual estimates are available. The upper panel of Figure 8 shows the corrected A and C distributions for our sample. Dashed lines define three morphological bins (ellipticals/ spirals/peculiars) drawn on the basis of similar measurements made on a local sample of galaxies of known morphology (Frei et al. 1996). Detailed consideration of this local dataset is deferred to the next section. To avoid confusion with the visual classifications, we will refer to the automated classes as AC -ellipticals ($AC - E$), AC -spirals ($AC - S$) and AC -peculiars ($AC - P$). The angle from the intersection point of the dashed line in the upper panel of Figure 8 to each point in the AC plane, defines a continuous classification angle, Θ . The correlation between this angle and the eyeball classifications is shown in the lower panel of the figure. Overall the agreement is satisfactory but a sizeable scatter is apparent. Note in particular that the angle does not distinguish well between early-type spirals and E/S0 galaxies.

4. Redshift-dependent Biases

High z galaxies imaged by the HST differ in appearance from their local counterparts because of their reduced apparent size and sampling characteristics, a lower signal-to-noise and reduced surface brightness with respect to the sky background, and a shift in the rest-wavelength of the observations. The latter term we will refer to as ‘bandpass shifting’. These effects will combine to give some uncertainty in the morphological classification of galaxies, generally in the sense of shifting objects to apparently later Hubble types.

Glazebrook et al (1995b) attempted to address this in the context of their visual classification procedure via a blind classification of local galaxies whose appearance was carefully simulated as viewed at a redshift $z = 0.7$. For machine classifications this has been addressed to some extent by Abraham et al. (1996b) using the parameters A and C . A benefit of working in the framework of A and C classifications is that it enables more quantitative statements about these biases.

In this paper we will extend the discussion begun by Abraham et al utilising the known redshifts of our sample to correct for these redshift-dependent biases. To do this we have relied on extensive simulations based on a set of multi-colour CCD images of local galaxies from Frei et al (1996). Our approach will be to assess (in various ways) the extent to which the A&C parameters for local galaxies of known type are likely to shift when they are placed at larger redshift. Statistically, over a number of galaxies, we then compare the distribution of classes, as viewed at a given redshift, with the intrinsic value at $z \approx 0$ to determine a ‘misclassification fraction’ for each type which is a function of redshift. The method assumes that the Frei et al galaxies of a given type are representative. Note, in particular, that we do not require an accurate sampling of the local morphological mix. Indeed, in principle, only a few representative galaxies of each type are required. Our goal and procedure differs from the synthetic creation of faint no-evolution samples (see eg. Bouwens, Broadhurst & Silk 1997) for which the Frei et al sample is not well suited.

4.1. The Frei et al Calibration Sample

The Frei et al sample consists of 82 galaxies with B_J and R CCD images, uniform in quality with foreground stars removed. It is important to note, however, that the Frei et al galaxies were not chosen with the intention of sampling the luminosity function of local systems uniformly. Indeed, Frei et al chose galaxies that are (a) bright, (b) have well-resolved morphological structures, and (c) span a wide range of Hubble system classification classes. It is therefore important to assess whether this sample is appropriate for calibrating redshift-dependent morphological trends.

The *absolute magnitude distribution* of the Frei et al sample is shown in Figure 9. The plot is based on M_B data published in the Revised Shapely Ames Catalog (RSA). We have applied an additional $0.^m5$ shift to take account of corrections applied for internal extinction in the RSA which we ignore in the CFRS+LDSS samples. We also indicate characteristic M^* values for local elliptical and Scd galaxies (Marzke et al. 1994). The Frei et al data peaks near M^* and, as expected, is deficient in systems ~ 2 mag or more fainter than M^* . This could be a drawback for our purposes, depending on how the morphological biases are corrected. If, for example, we correct morphologies back to those appropriate for the rest-frame I -band, a proper match between the CFRS/LDSS and Frei et al luminosity distributions is more important at high redshift. In this case, the majority of our survey galaxies beyond $z \simeq 0.3$ are drawn from within two magnitudes of M^* . In Figure 9 we show lines corresponding to the apparent magnitude limits for the CFRS survey based on k -corrections for early and late-type systems. Clearly the underluminous galaxies which are deficient in the Frei sample are undetectable. For our approach this leads to a low number of objects, and hence a large statistical uncertainty. But since we cover the whole range of morphological types, we do not introduce any systematic biases.

One might worry that selecting the galaxies to be nice and regular looking might lead us to infer less bandshifting than is observed. However, we do not think this is a major problem for our

approach, since the comparison with the low-redshift data effectively takes out the actual values of A and C . Thus, although the Frei *et al* sample is useful for estimating the apparent shift in morphology with redshift for regular objects of suitable luminosity, it could be improved. Future imaging surveys of local systems should aim to sample fairly the *distribution* of morphological types within both the luminosity selection criteria of the survey and the regions on the A vs. C diagram. Such datasets would also allow compilation of no- and mild-evolution simulated datasets for comparison with high redshift data (see also Bouwens *et al.* 1997).

4.2. Wavelength-dependent Trends

The simplest test we can perform is to measure the A and C parameters defined earlier in both the R and B_J -band images of the Frei *et al* galaxies. Since our faint HST images are taken with the F814W filter, we effectively see the R band at a redshift of 0.2 and the B_J band at a redshift of 0.87. The shift in A and C across the Frei *et al* sample is thus a crude but simple measure of the shift arising from the bandpass effect over much of the redshift range sampled.

In the top panel of Figure 10 we plot the change in asymmetry A observed using the R and B_J images of the same local galaxy. Late-type systems are denoted by filled circles and, as expected, there is a clear trend for such systems to have larger asymmetry at shorter wavelengths where the star-formation signatures are more irregular. However, in quantitative detail, the size of the effect is quite small. The corresponding shift in concentration C , shown in the bottom panel, is somewhat larger. The change in C required for a galaxy to cross the AC -peculiar and AC -elliptical boundary is also indicated on the figure; for the AC -peculiars this is strongly dependent on asymmetry.

This simple comparison indicates that only a small fraction of the Frei *et al* galaxies would cross into the areas defining different morphological types. However, the comparison is crude and takes no account of more complex sampling and noise effects.

4.3. Results from Detailed Simulations

To quantify the redshift biases more precisely, we decided to incorporate each of the effects that combine to give the final HST appearance. The method adopted is based on that described in more detail by Abraham *et al.* (1997) and can be summarised as follows:

- For each pixel we calculated the $B_J - R$ colours; to avoid edge effects we smoothed the images slightly before calculating the colours.
- The pixel $B_J - R$ colours were then used to select an SED to each pixel (as for the integrated colours discussed earlier). This SED was then used to determine the k-correction applicable to each pixel.

- The final step is to rebin the image, using the known and wanted redshift, applying $(1+z)^4$ surface brightness dimming and adding noise corresponding to the characteristics of WFPC–2 for our mean exposure time.

For each redshift we only analysed those redshifted galaxies that would have been selected into either the CFRS or LDSS–2 redshift surveys. Beyond $z \simeq 0.9$, however, only a few of the Frei *et al* galaxies would be seen; this is because the bright galaxies in the Frei sample tend to be Sab galaxies whose k-corrections are substantial when the 4000Å break enters the I-filter (this is also indicated in Figure 9). This leads to a small number of galaxies, and hence an increase in the statistical uncertainties. To rectify this problem, we adopted an alternative approach. We selected the Frei *et al* galaxies that would have had $I_{AB} < 23.50$, ie. one magnitude too faint, and brightened these galaxies so that they fell within our selection criteria. This led to an average brightening of $\langle M_B \rangle \approx 1.5$ magnitudes, and kept $M_B \geq -22.5$. This enabled us to get a satisfactory number of objects without introducing any over-luminous objects. Provided the morphological characteristics do not vary significantly over this small luminosity range, this should not affect our conclusions.

The aim of the detailed simulations is to determine that fraction of a given type of Frei *et al* galaxy which *appears* to be of a different morphological type (as measured by A and C) at a chosen redshift z . For convenience we will denote the number of objects in a given category by N with superscript 'obs' for the observed number and no superscript for the true number in that class. We connect these two numbers via a drift coefficient, \mathcal{D}_{XY} which characterises the drift from category X to category Y, defined as

$$\mathcal{D}_{XY} = \frac{N_{X \rightarrow Y}}{N_X}, \quad (2)$$

where $N_{X \rightarrow Y}$ is the number of objects of class X that are classed as Y at a higher redshift. From the simulations we can estimate \mathcal{D}_{XY} for various redshifts.

This methodology is similar to that of the k-correction applied to convert an observed magnitude into a rest-frame value. The ultimate aim here is to recover the *rest-frame morphology*. Although the analogy fails in detail because of the added complications of distance-dependent resampling and surface brightness dimming, our simulations indicate that these are second order effects. If the central concentration is corrected for surface brightness effects as described in section 3.2, the dominant cause of a migration to a different morphological type is the pixel-by-pixel k-correction.

The analogy with the k-correction suggests two approaches for analysing our data. Given we have R -band images of the Frei galaxies and the local morphological studies are done in B , it seems natural to correct our HST morphologies to those appropriate for the rest-frame B_J -band. As we observe this rest wavelength directly at $z \approx 0.9$, the corrections would be small at high redshift but larger at low redshift. A problem with this approach is that our benchmark sample is

not ideal for studying the morphological shifts at the low luminosities appropriate for the nearby objects, due to the low number of faint galaxies.

The alternative approach is to correct our HST morphologies to rest frame R assuming, as seems reasonable, that the morphology changes little between rest-frame I and R . In this case, nearby, intrinsically faint galaxies, need no correction and although a larger correction is needed at high redshifts, in this case the Frei *et al* sample is well matched in luminosity. Neither approach is perfect, but we consider the latter to be more reliable until larger, multiband local samples are available. We will therefore concentrate on applying corrections to rest-frame R morphologies (although, for completeness, we tabulate drift coefficients appropriate for rest-frame B_J).

The results of this exercise are summarised in Table 4. The numbers here are consistent with the earlier discussion of the change in C from the R to B_J -band images but we consider the results to be more reliable given the more detailed treatment of the effects of sampling and background noise. In particular, the drift coefficients calculated from R to B_J band images agree excellently with the ones found here. The drift coefficients not listed were all found to be zero in the simulations.

We can relate the observed number of objects in class X to the true number through

$$N_X^{obs} = N_X + \sum_{Y \neq X}^{\text{Classes}} N_Y \mathcal{D}_{YX} - N_X \sum_{Y \neq X}^{\text{Classes}} \mathcal{D}_{XY}. \quad (3)$$

Equations (3) can be readily solved given the observed number of galaxies.

Broadly speaking, there are two dominant effects. First there is an apparent migration from *AC*-spirals to *AC*-peculiars if we classify galaxies from observed I -band images. This bias is expected to occur also for eyeball classification. At $z = 0.7$ we can expect only 13% of the *AC*-spirals to be misclassified as *AC*-peculiars, whereas by $z = 0.9$ the misclassified fraction grows to 24%. Presumably this trend continues at higher redshift. Due to the restrictions in the local dataset discussed above, we have not extended the simulations beyond $z = 0.9$. U-band imaging would be highly desirable to quantify bandshifting beyond $z = 1$ (see also Hibbard & Vacca 1997)

In addition there is a strong trend for *AC*-ellipticals to be migrate into the *AC*-spiral category. The net result is somewhat less clear as there is also a drift in the opposite sense (from *AC*-*S* into *AC*-*E*) due to random measurement errors on C where the boundary is nearly vertical.

From the errors in Table 4 it is evident that the drift coefficients are uncertain. A larger sample of calibrating galaxies is clearly required to make more precise statements about the drift coefficients. Nevertheless, the principal conclusion of the simulations is a reasonably precise measure of the proportion of high redshift *AC*-peculiars which are likely to be genuine spiral galaxies. The mixture of regular spirals and spheroidal galaxies should be faithfully observed with HST out to redshifts $z \simeq 1$, however with a likely loss of *AC*-*E* at high redshift which might be able to make up for the loss of *AC*-spirals to the *AC*-*P* category. A montage of the *AC*-peculiars sorted by redshift and rest-frame [O II] equivalent width is shown in Figure 11.

5. Analysis

The first question we address relates to luminosity evolution as a function of galaxy class inferred independently from the MDS and ground-based surveys. We wish to understand these results in the context of the morphologically-segregated redshift distributions and luminosity functions (LFs) now available to us. Such results are of considerable interest, as recent semi-analytical models (Baugh et al. 1996; Shimasaku & Fukugita 1997) already claim to reproduce observed trends in the global star formation history based on ground-based redshift surveys and Lyman limit selected samples in the Hubble Deep Field (Madau 1997). However, a physical understanding of these trends in the context of these models demands a more detailed comparison such as is now possible for each of the various morphological types. Although hierarchical assembly may transform late-type systems into more regular spheroidal and disk galaxies, in principle these effects can be incorporated in such models.

In discussing the observational results, as mentioned in Section 2, we will concentrate only on that subset of the survey containing objects from the LDSS-2 and CFRS surveys. This provides a total of 249 galaxies with secure redshifts $z < 1.2$. In order to implement the quantitative results on redshift-dependent biases from the previous section, we will restrict discussion to types based on the *AC*-classifications. For 12 objects whose isophotal area is less than 64 pixels, or whose images lie within the planetary camera, the *A* and *C* measurements were replaced with eyeball classifications. One galaxy among the 249 was classed as compact. Given the uncertainty associated with dealing with such an object, we increased the error bar in the relevant redshift range accordingly. In total, there are 24 spectroscopically-confirmed stars, four QSOs with $z > 1.2$ and 35 objects with uncertain redshift (note=1) or no redshift estimate at all. The failures have been ignored in the analysis (and would not change the main conclusions below if included).

5.1. Redshift distributions

It will be helpful in discussing the observed type-dependent redshift distributions, $N(z)$, to have no-evolution predictions based on local LFs. To make these predictions we adopted type-dependent Schechter LFs listed in Table 5. For the spirals and ellipticals, these are updated versions of those used by Glazebrook et al. (1995b) with ϕ^* adjusted to give the observed fractions given by Shanks et al. (1984) in their $b_J < 16.7$ sample. For the irregular/peculiar galaxies we have adopted the late-type/irregular LF given by Marzke et al. (1994). Using these local LFs and the *k*-corrections discussed earlier, we calculate $N(z)$ for the LDSS2 and CFRS galaxies using the selection criteria and areas listed in Table 3. For the spiral and spheroidal galaxies, we are primarily interested in the luminosity scales at the bright end and so even though there are considerable uncertainties in the local LFs, the predictions based upon them are nonetheless a useful guide.

As well as indicating the expected $N(z)$ distributions for the combined CFRS and LDSS-2

magnitude limits, appropriately weighted for the sample sizes involved, we also calculate the effect on the distribution of a luminosity evolution equivalent to a linear shift in M^* with redshift that amounts to one magnitude at $z = 1.0$. We will refer to this prediction as ‘mild evolution’. We then determined the observed number of objects as a function of AC -class in each redshift bin fully incorporating the effects of morphological bias as determined in the previous section using equation (3). Since the local morphological mix for the luminosity functions is based on B -band morphologies, we use the \mathcal{D}_{XY} values for correction to B_J -band morphologies, taken from Table 4. The $N(z)$ distributions for the various types of AC class are compared with the no-evolution and mild evolution predictions in Figure 12.

Figure 12 shows that, taking into account the biases discussed above, the number of high z ellipticals and spirals is broadly consistent with the expectations based on $N(m)$ counts. Given the limited size of our survey, the possibility of incompleteness and, especially, the reliance that has to be made on the local LF normalisation in such comparisons, it is difficult to make a precise statement on the extent of any luminosity evolution. A K-S test applied to the elliptical $N(z)$ is unable to distinguish between the no evolution and mild evolutionary predictions. The size of the spiral sample is larger but precise conclusions are difficult to obtain because of the number of spirals without redshifts. Even so, the mild evolutionary case is preferred: the no evolution $N(z)$ is rejected at the 97% level and this confidence level would be stronger if the failures are at high redshift as is most likely the case. The drop in numbers past $z = 1$ is most likely due to incompleteness in the redshift determinations (see also Cowie et al. 1996).

The most convincing result apparent from Figure 12 is the very considerable excess population of AC -peculiars beyond $z \simeq 0.4$ which cannot be explained through residual uncertainties in the misclassification fraction as applied to the regular spirals. The figure shows quite clearly how the large excess population recognised from early ground-based studies arises primarily from these sources. Note also that the *form* of the redshift distribution is skewed to high redshift and thus a mistaken normalisation in the local LF would not be helpful in reconciling the data with the simple model predictions. The result is highly suggestive of an evolutionary effect. Although it is important to remember that the AC -peculiar category may include a variety of physical types (see in particular the discussion of $I - K$ colours of these objects in Glazebrook et al. 1997) and that, in principle, morphology itself may be a transient phenomenon, understanding the strong redshift dependence in the abundance of the AC -peculiars is clearly a crucial goal for making progress.

5.2. Luminosity functions

The previous section exploits one aspect of the $M_B - z$ plane to discuss the properties of the survey galaxies, but a disadvantage in the interpretation of Figure 12 is the need to assume a local LF and particularly its normalisation. In order to understand *how* the population of AC -peculiars evolves so dramatically to provide the excess population, and to complement the study of AC -*S* and AC -*E*, it is therefore valuable to consider the form of the luminosity function at various

redshifts. This can be calculated for the HST survey galaxies using a V_{\max} formalism.

As the CFRS and LDSS surveys have quite different selection criteria, we utilise an approach similar to that adopted by Ellis et al. (1996). For each galaxy in the survey, V_{\max} was calculated using

$$V_{\max,i} = \sum_j^{\text{Surveys}} V_{ij},$$

where V_{ij} is the normal accessible volume of galaxy i in survey j . To cope with the different selection criteria in the two surveys, estimates of the b_J magnitudes of the CFRS galaxies and I_{AB} magnitudes of the LDSS-2 galaxies are required. For the LDSS-2 objects we used the HST 3" magnitudes and converted these to I_{AB} following methods discussed above. For the CFRS objects we calculated b_J magnitude synthetically from V photometry similarly. The method was then checked for a subset for which B_{AB} photometry was available and a good agreement was found. For consistency, colour terms were calculated using the same interpolated SEDs that were used for the calculation of the absolute magnitudes. The effective areas were taken from Table 3. The LFs estimated in this way are plotted for three redshift bins in Figure 13. Error bars were determined using bootstrap resampling techniques.

The redshift biases determined in Section 4.3 were incorporated in a simple fashion. We only took account of the shift of *AC*-spirals into the *AC*-peculiar category in the highest redshift bin. We then assigned 24% of the *AC*-peculiar to the *AC*-spiral class, for each bootstrap repetition. The effects are not significant in the following discussion.

A major disadvantage of multi-object redshift surveys with narrow ranges in apparent magnitude is that they provide very little overlap in LF across the different redshift bins. Nonetheless, the figure shows that the LFs for *AC*-ellipticals do not exhibit *strong* evolution. The *AC*-spiral LFs show a shift of ≈ 1 magnitude to $z = 1$ but the greater component occurs between the two lower redshift intervals. The LFs for the *AC*-peculiars clearly does show substantial evolution from $z = 0$ to $z = 1$, in the sense of either a dramatic brightening with redshift or a substantial increase in the volume density of luminous examples. It is difficult to quantify this evolution precisely because of the lack of overlap between the various redshift bins. In particular we do not observe *any* luminous *AC*-peculiar galaxies in the lower redshift bin, even though they should be detected given our magnitude limits. However, as with the redshift distributions, it seems that the apparently declining population of luminous *AC*-peculiars is the dominant effect (as originally proposed by the MDS team), but with a significant contribution also from the *AC*-spirals.

5.3. Luminosity densities

We now attempt to quantify the extent to which the evolution we have found for the *AC*-peculiars contributes to that observed for the overall population. Numerous authors (Lilly

et al. 1996; Madau et al. 1996; Madau 1997) have expressed the overall evolution of the galaxy population in terms of a rest-frame luminosity density or a volume-averaged star formation rate as a function of redshift. Over the redshift range $0 < z < 1$, these articles interpret the observations in terms of a substantial decline in star-formation activity at recent times. A crucial question is whether virtually all of this decline arises from the rapidly-evolving irregular component discussed above.

We can address this by examining the rest-frame $B(AB)$ luminosity density of the galaxies in our HST survey as a function of morphological type. The results of this exercise are shown in Figure 14 where the errors bars are obtained through bootstrap resampling as before. To correct for the fact that we observe only a limited magnitude range, we fit Schechter functions to the luminosity functions in Figure 13, with the faint end slope fixed to $\alpha = -0.5$ for the AC-E and $\alpha = -1$ for AC-S and AC-P. It is clear from that figure that this leads to considerable uncertainties. In particular the fit for AC-P in the low redshift bin is too uncertain to be useful. The corrected values have been plotted as open symbols in Figure 14.

Since the correction for *AC*-peculiars at low redshift is unknown, one could argue that their rapid rise in the blue light density is just an artifact of the limited magnitude range sampled at low redshift. However, it is interesting to note from Figure 13 that we do not see any bright *AC*-peculiars, *even though they would lie within the selection criteria*. This constrains the luminosity function for this region, and a conservative upper limit to the correction factor is 1.5. Thus we would argue that the rapidly-increasing contribution to the blue light by the *AC*-peculiars is a robust result. Over $z \simeq 0.3-0.9$ this class provides an order of magnitude increase in the detected luminosity density in a given magnitude limited sample, consistent with their dominant effect of the HST galaxy counts over the range detected by the surveys. The *AC*-spirals contribute smaller amount to the overall evolution. Their contribution is not so evident in the HST galaxy counts, and can be attributed to our being able to correct for redshift-dependent effects in the classifications. At high redshift, galaxies would be assigned too low C values, due to surface brightness dimming. The correction in Appendix A rectifies for this and hence demonstrates the importance of allowing for redshift dependent effects.

5.4. The physical nature of the star-forming galaxies

Given that galaxies of irregular morphology are rapidly evolving with redshift in their abundance and/or mean luminosity (and hence detected luminosity density), and that this trend appears to dominate the evolution we see, at least in the context of galaxy counts selected according to apparent magnitude, these remarkable systems clearly hold the key to understanding the rapid demise in star formation activity since $z \simeq 1$.

A basic question we must address is whether this category represents a single type of object evolving in isolation, perhaps fading in luminosity after an energetic burst of activity, or are we

witnessing the gradual transformation of galaxies, rendered irregular in form simply by virtue of their enhanced star formation, into more regular systems? Progress might be made on this question if it could robustly be demonstrated that the rapid evolution seen in the *AC*-peculiars does or does not occur at the expense of accompanying changes in the regular spirals. That the high redshift volume density of spirals is consistent with local estimates does imply, at first sight, that the *AC*-peculiars might evolve independently of the more modest changes that affect the spirals. Of course, a decline in star formation activity in a long-lived class e.g. the spirals, will most likely be accompanied by a drop in luminosity and such transformations may not always occur above the detection limits of the survey so it is difficult to use this argument with confidence. Also, conclusions derived on the basis of number conservation are uncertain in our case given our small sample size and the remaining effects of redshift incompleteness. Greater progress may be possible in constraining the growth of the spiral population by attempting to examine a well-defined subset taking due care to allow for the effects of size and surface brightness. This is the approach adopted in Paper II.

Finally, as we have emphasised, in morphological terms, the *AC*-peculiars represent a mixture of very different objects (Figure 11). The category includes some very late-type spirals whose asymmetries and central concentrations place them in the *AC* plane normally occupied by low z irregulars, double systems most likely in the act of merging and other peculiar systems which defy classifications in the normal Hubble sequence. Paper IV in this series examines the structure properties and merger statistics in an attempt to quantify the dominant sub-processes that may drive the evolution in this class.

Examination of Figure 11 suggests that a significant fraction of the *AC*-peculiars with high [OII] equivalent widths appear to be rather compact. These could be the more extreme examples of the star-forming population which dominates the evolutionary trends discussed above. In this context, it is interesting to consider Guzman et al's (1997) claim that a considerable fraction of the star formation activity seen at high redshift occurs in “compact” galaxies. The compact galaxies in their study were selected within the Hubble Deep Field flanking fields on the basis of apparent magnitude, angular size and average surface brightness. Although their sample is somewhat smaller than that analysed here, both their magnitude and surface brightness limits are generally fainter. However, our HST exposure times are generally longer.

A key point in understanding Guzman et al's result in the context of this paper where the bulk of the evolution occurs in galaxies of irregular morphology is the precise definition of a “compact” galaxy. Guzman et al adopted a half light radius $r_{1/2}$ of less than or equal to 0.5 arcsec as well as a surface brightness selection criterion (Phillips et al. 1997). We can ask how many of our regular and irregular galaxies would fulfill this compactness criterion at various redshifts. From our data we find that as many as 37% of the *AC*-spirals and 26% of *AC*-peculiars beyond $z=0.5$ have $r_{1/2} < 0.5''$ and $\mu_{F814} > 22.24$.

The comparison can continue by examining the volume-averaged star formation rate (SFR)

for the galaxies detected in our survey based, as in Guzman et al, on the measurements of the equivalent width (EW) of [OII] and the relation between EW[OII] and SFR from Guzman et al. (1997),

$$\text{SFR}(M_{\odot}\text{yr}^{-1}) \approx 2.5 \times 10^{-12} \times 10^{-0.4(M_B - M_{B\odot})} \text{EW}_{[\text{OII}]} . \quad (4)$$

This corresponds to $(U - V)_{AB} = 0.7$ in the simple model of Hammer et al. (1997) — a colour which is representative for the galaxies in the higher redshift interval.

Adopting the same redshift intervals as for the luminosity density and LFs, we show the results based on equation (4) in Figure 15. It is interesting to note how closely this figure corresponds to Figure 14. Relative to low redshift, the *AC*-peculiar category cause the strongest evolution even though the evolution in the *AC-S* and *AC-P* categories is comparable at high redshift. As before, the absolute values are highly uncertain, both because they refer only to the detected population but also because of the approximate conversion of [OII] to SFR (see in particular the extensive discussion of the properties of the CFRS objects in Hammer et al. 1997). Nonetheless, the strong morphological trends are clear. Finally, we note that the galaxies in our sample satisfying the Guzman et al. selection criteria contribute 26% of the star formation rate between $z = 0.5$ and $z = 1.0$. This is in reasonable agreement with Guzman *et.al*'s results when the fact that their survey goes 1.7 magnitudes fainter than ours is taken into account.

In summary, there seems to be reasonable agreement between ourselves and Guzman et al. in the physical properties of the faint galaxies claimed to dominate the evolutionary trends. The overlap with our own result is understandable, although we would argue no great significance can be attached to the label ‘compact’ e.g. in considering the present day equivalent of such systems or in describing the sources in Figure 11.

6. Conclusions

We have analysed the HST images of 341 galaxies drawn from both the CFRS and Autofib/LDSS ground-based redshift surveys. Our catalogue includes new spectroscopy of a magnitude-limited sample in the Groth strip. In this, the first paper in this series, we have analysed the HST data, in conjunction with the available spectroscopic redshifts, in order to understand the evolutionary trends identified independently from the morphological studies in the Medium Deep Survey and from the redshift-dependent luminosity functions derived from our two extensive ground-based redshift surveys.

We summarise our findings as follows:

- We have extended the automated classification scheme developed by Abraham et al. 1996b which places galaxies in 3 broad categories (ellipticals/spirals/peculiars) and quantified, via simulations and other tests, the likelihood of misclassification when such systems are viewed at high redshift. For the typical HST exposure times involved in this survey, systematic

misclassifications occur in the sense of shifting normal galaxies to apparently later Hubble types at fixed *observed* wavelength. We quantify how this can be taken into account when redshifts are available.

- Taking these biases into account, we demonstrate that the number redshift relation for regular *AC*-ellipticals is consistent with expectations on the basis of no evolution or ‘mild’ evolution (corresponding to a magnitude of luminosity evolution by a redshift 1). However, the numbers are too small to differentiate these possibilities. In the case of the *AC*-spirals, models incorporating mild evolution are preferred, and the luminosity function indicate luminosity evolution of about 1 magnitude to $z \sim 1$.
- The number of galaxies with irregular morphology increases with redshift well beyond what is reasonable to expect on the basis of systematic misclassifications of spirals. We conclude there is a significant evolutionary signal confined to this population. Analyses based on the luminosity density and luminosity functions divided by morphological class confirms that the demise in the *AC*-peculiar population is a dominant component in the recent evolution of the galaxy population.
- There is no obvious decline with redshift in the abundance of regular galaxies as might be the case if the *AC*-peculiar population is transforming into more familiar systems. However, this conclusion is not particularly robust given it relies on uncertain volume densities in our modest sample. Such quantitative interpretations are also hampered by the fact that the classifications may well be transient and that luminosity fading may remove systems from the sample at lower redshift. A variety of different physical sources may contribute to the peculiar category (including misclassified late-type spirals, genuine irregulars, merging systems and starburst galaxies).

We acknowledge useful discussions with Simon White, Carlos Frenk, Joe Silk and Alan Dressler. We also acknowledge the invaluable contributions provided by all STScI staff involved in the HST project. JB was supported by The Research Council of Norway, project number 107798/431. Bob Abraham acknowledges support from PPARC.

REFERENCES

Abraham, B., Freedman, W., Madore, B. 1997 In The proceedings of the 36th Herstmonceux conference, “HST and the high redshift universe”, eds: Tanvir, N., Aragon-Salamanca, A., & Wall, J. V. (World Scientific:Singapore)

Abraham, R. G., Tanvir, N. R., Santiago, B. X., Ellis, R. S., Glazebrook, K., van den Bergh, S. 1996a, MNRAS, 279, L47

Abraham, R. G., Valdes, F., Yee, H. K. C., van den Bergh, S. 1994, *ApJ*, 432, 75

Abraham, R. G., van den Bergh, S., Ellis, R. S., Glazebrook, K., Santiago, B. X., Griffiths, R. E., Surma, P. 1996b, *ApJS*, 107, 1

Baugh, C. M., Cole, S., Frenk, C. S. 1996, *MNRAS*, 282, L27

Bouwens, R., Broadhurst, T., Silk, J. 1997, preprint astro-ph/9710291

Colless, M., Ellis, R. S., Broadhurst, T. J., Taylor, K., Peterson, B. A. 1993, *MNRAS*, 261, 19

Cowie, L. L., Songaila, A., Hu, E. M., Cohen, J. G. 1996, *AJ*, 112, 839

Crampton, D., Le Fèvre, O., Lilly, S., Hammer, F. 1995, *ApJ*, 455

Driver, S. P., Windhorst, R. A., Griffiths, R. E. 1995a, *ApJ*, 453, 48

Driver, S. P., Windhorst, R. A., Ostrander, E. J., Keel, W. C., Griffiths, R. E., Ratnatunga, K. U. 1995b, *ApJ*, 449, L23

Ellis, R. S. 1995 in IAU Symposium 164, ed van der Kruit, P. & Gilmore, G., 291

Ellis, R. S., Colless, M., Broadhurst, T., Heyl, J., Glazebrook, K. 1996, *MNRAS*, 280, 235

Frei, Z., Guhathakurta, P., Gunn, J. E. 1996, *AJ*, 111, 174

Gehrels, N. 1986, *ApJ*, 303, 336

Glazebrook, K., Abraham, R., Santiago, B., Ellis, R., Griffiths, R. 1997, preprint

Glazebrook, K., Ellis, R., Santiago, B., Griffiths, R. 1995a, *MNRAS*, 275, L19

Glazebrook, K., Ellis, R. S., Colless, M., Broadhurst, T., Allington-Smith, J., Tanvir, N. 1995b, *MNRAS*, 273, 157

Griffiths, R. E., et al., *A. J.* 1994, *ApJ*, 435, L19

Groth, E. J., Kristian, J. A., Lynds, R., O’Neil, Earl J., J., Balsano, R., Rhodes, J., Idt, W. 1994, *BAAS*, 185, 5309

Guzmán, R., Gallego, J., Koo, D. C., Phillips, A. C., Lowenthal, J. D., Faber, S. M., Illingworth, G. D., Vogt, N. P. 1997, *ApJ*, 489, 559

Hammer, F., et al., *ApJ*, 481, 49

Heyl, J., Colless, M., Ellis, R. S., Broadhurst, T. 1997, *MNRAS*, 285, 613

Hibbard, J. E., Vacca, W. D. 1997, *AJ*, 114, 1741

Holtzman, J. A., Burrows, C. J., Casertano, S., Hester, J. J., Trauger, J. T., Watson, A. M., Worthey, G. 1995, PASP, 137, 1065

Le Fèvre, O., Crampton, D., Lilly, S. J., Hammer, F., Tresse, L. 1995, ApJ, 455, 60

Le Fèvre, O. et al. 1997, in preparation (Paper IV)

Lilly, S. et al. 1997, accepted ApJ

Lilly, S., Le Fèvre, O., Hammer, F., Crampton, D. 1996, ApJ, 460, L1

Lilly, S. J., Le Fèvre, O., Crampton, D., Hammer, F., Tresse, L. 1995a, ApJ, 455, 50

Lilly, S. J., Tresse, L., Hammer, F., Crampton, D., Le Fèvre, O. 1995b, ApJ, 455, 108

Madau, P. 1997, preprint, astro-ph/9707141

Madau, P., Ferguson, H. C., Dickinson, M. E., Giavalisco, M., Steidel, C. C., Fruchter, A. 1996, MNRAS, 283, 1388

Marzke, R. O., Geller, M. J., Huchra, J. P., Harold G. Corwin, J. 1994, AJ, 108(2), 437

Naim, A., et al., MNRAS, 274, 1107

Odewahn, S. C., Windhorst, R. A., Driver, S. P., Keel, W. C. 1996, ApJ, 472, L13

Phillips, A. C., Guzmán, R., Gallego, J., Koo, D. C., Lowenthal, J. D., Vogt, N. P., Faber, S. M., Illingworth, G. D. 1997, preprint

Schade, D. et al. 1997, in preparation (Paper III)

Schade, D., Lilly, S. J., Crampton, D., Hammer, F., Le Fèvre, O., Tresse, L. 1995, ApJ, 451, L1

Shanks, T., Stevenson, P. R. F., Fong, R., Macgillivray, H. T. 1984, MNRAS, 206, 767

Shimasaku, K., Fukugita, M. 1997, preprint

van den Bergh, S. 1998, in preparation

White, S. D. M. 1996, In Science with Large Millimetre Arrays, ed: Shaver, P., ESO Astrophysics Symposia (Berlin Springer), 33

A. Correction of C

A primary advantage of the use of the asymmetry and concentration indices (A and C) in our survey, compared to its equivalent application to the Medium Deep Survey data, is that redshifts are available for all the galaxies in the sample. It is therefore of interest to consider how to optimise the measurement of these parameters to account for the variation of the limiting rest isophote.

In measuring C , a limiting isophote, μ_l , is selected relative to the background sky. Since the HST images generally have similar limiting isophotes regardless of the galaxy redshift, in the rest-frame there are shifts with redshift which scale as $10 \log(1 + z)$. To correct for this effect, one can either attempt to measure C to the same rest-frame isophote, or one can correct the measurements with an average shift calibrated with simulations. The former approach has the disadvantage of discarding information at low redshift since, to maintain uniformity, the adopted rest-frame threshold must be set fairly high to accommodate the high z images. Given the large redshift range in our sample, the latter approach is preferred. For symmetric light profiles the central concentration is given by:

$$C = \frac{f(0.3R)}{f(R)}, \quad (\text{A1})$$

where R is the radius at which the surface brightness is equal to the limiting isophote selected, and $f(R)$ is given by:

$$f(R) = 2\pi \int_0^R I(r) r dr.$$

Equation (A1) can be calculated exactly for a pure de Vaucouleurs law,

$$I(r) = I_e \exp \left(-7.67 \left((r/r_e)^{1/4} - 1 \right) \right).$$

The resultant expression for the central concentration is then

$$C_{dV} = \frac{g(V)}{g(0.3^{1/4}V)}, \quad V = 7.67 \left(\frac{\mu_l - \mu_e}{8.3276} + 1 \right), \quad (\text{A2})$$

with $g(V)$ being given by

$$g(V) = \int_0^V v^7 e^{-v} dv = 7! \left[1 - e^{-x} \sum_{k=0}^7 \frac{x^k}{k!} \right].$$

It is worth noting that the expression for C is independent of details of the profile except for the central surface brightness or, equivalently, the surface brightness at the effective radius. This statement remains true for exponential disks, but breaks down for mixed profiles, where both the exponential scalelength and the effective radius come into play.

Accordingly, we therefore have a relation that can be used to calculate the change in C that occurs as a function of redshift: $\Delta C = g(z = 0; \mu_0) - g(z = z; \mu_0)$. This is a function of the details of the profile, but not strongly so. In practice, we used the functional form and calibrated the correction from the redshifted Frei et al images (see section 4.2). This enabled us to adopt the following relation to correct C :

$$\Delta C(z) = 0.6 \times [C_{dV}(0; \mu_0 = 15.0) - C_{dV}(z; \mu_0 = 15.0)], \quad (\text{A3})$$

with C_{dV} given in equation (A2) above. We will refer to this as a *minimal* correction as it does not take into account bandshifting effects, and it has been applied to all C values in this paper.

Table 1. HST Imaging Survey

Field ^a	Red filter	Integration time (s)	NCOMB ^b	Blue filter	Integration time (s)	NCOMB ^b	<i>N</i> _{targets} ^c	<i>N</i> _z ^d	<i>N</i> _{star} ^e
cfrs_03_1	F814W	6700	5	14	13	0
cfrs_03_2	F814W	6700	5	15	14	0
cfrs_03_3	F814W	6700	5	13	10	0
cfrs_03_4	F814W	6400	6	F450W	6600	6	11	11	0
cfrs_03_5	F814W	6400	6	F450W	6600	6	5	5	0
cfrs_10_1	F814W	6700	5	17	16	1
cfrs_10_2	F814W	6700	5	12	11	1
cfrs_10_3	F814W	5302.5	4	24	20	2
cfrs_14_1	F814W	7400	6	F450W	7800	6	21	21	0
cfrs_14_2	F814W	7400	6	F450W	7800	6	13	10	3
cfrs_22_1	F814W	6700	5	8	7	0
cfrs_22_2	F814W	6700	5	14	12	0
cfrs_22_3	F814W	6700	5	15	13	1
grth_14_1	F814W	4400	4	F606W	2800	4	36	31	4
grth_14_2	F814W	4400	4	F606W	2800	4	16	12	4
grth_14_3	F814W	4400	4	F606W	2800	4	21	17	1
grth_14_4	F814W	7400	6	F450W	7800	6	20	20	0
grth_14_5	F814W	4400	4	F606W	2800	4	18	14	3
grth_14_6	F814W	4400	4	F606W	2800	4	11	10	1
ldss_10a	F814W	5800	5	F380W	6000	6	13	10	1
ldss_10b	F814W	5800	5	F380W	6000	6	18	13	2
ldss_10c	F814W	5800	5	F218W	6000	6	10	7	2
ldss_13a	F814W	5800	5	F380W	6000	6	13	6	2
ldss_13b	F814W	5800	5	F380W	6000	6	21	15	1
ldss_13c	F814W	5800	5	F380W	6000	6	15	8	2
Total ^f						341	269	44	28

^acfrs_03=CFRS 3^h field, grth_14=Groth 14^h field, ldss_10a=LDSS-2 10^h.

^bThe number of individual exposures combined to form the final image

^cThe number of spectroscopic targets in the field

^dThe number of objects with reliable redshift measurement (note>1)

^eThe number of stars

^fThere is some overlap between the different frames so the total is not the sum of the columns

Table 2. Data for objects in the survey

ID	z	F814W	$M_{B_{AB}}$	Note ^a	Class ^b	A ^c	C ^c	AC-Class ^d	$EW_{[OII]}$ (1σ) ^e	Origin	Old ID ^f
03.0035	0.880	21.50	-22.06	1	4	0.080	0.319	4	...	CFRS	...
03.0315	0.223	20.54	-18.86	4	5	0.079	0.257	4	46(3)	CFRS	...
03.0316	0.815	22.26	-20.91	3	4	0.081	0.202	4	12(2)	CFRS	...
03.0321	...	21.87	...	0	2	0.123	0.418	1	...	CFRS	...
03.0327	0.606	21.86	-20.34	3	6	0.119	0.349	4	27(4)	CFRS	...
03.0332	0.188	21.92	-17.62	4	4	0.065	0.216	4	14(3)	CFRS	...
03.0337	0.360	22.31	-18.86	3	1	0.085	0.474	1	22(10)	CFRS	...
03.0346	...	21.79	...	0	4	0.165	0.418	4	...	CFRS	...
03.0358	0.088	17.31	-19.95	3	2	0.416	0.550	1	...	CFRS	...
03.0365	0.219	19.32	-20.08	4	3	0.060	0.449	1	32(5)	CFRS	...
03.0384	...	21.63	...	0	6	0.237	0.441	6	...	CFRS	...
03.0443	0.118	19.55	-19.50	4	1	0.103	0.564	1	...	CFRS	...
03.0445	0.530	20.80	-21.55	3	5	0.060	0.220	4	10(1)	CFRS	...
03.0466	0.534	23.14	-19.59	3	4	0.034	0.198	4	29(4)	CFRS	...
03.0480	0.608	22.24	-20.32	3	4	4	99(13)	CFRS	...
03.0485	0.606	21.53	-20.24	4	6	0.148	0.146	6	78(16)	CFRS	...
03.0488	0.607	21.43	-20.86	4	6	0.276	0.100	6	66(11)	CFRS	...
03.0523	0.651	21.28	-21.22	4	6	0.313	0.382	4	38(10)	CFRS	...
03.0528	0.714	21.36	-21.23	3	3	0.058	0.370	4	...	CFRS	...
03.0560	0.697	21.34	-21.06	3	2	0.079	0.425	1	11(1)	CFRS	...
03.0579	0.660	22.12	-20.47	2	4	0.107	0.236	4	5(5)	CFRS	...
03.0595	0.606	21.57	-20.80	4	8	0.276	0.133	6	17(1)	CFRS	...
03.0599	0.480	21.19	-20.63	4	5	0.111	0.158	4	41(5)	CFRS	...
03.0717	0.607	20.93	-21.18	3	5	0.048	0.254	4	4(4)	CFRS	...
03.0982	0.195	21.30	-18.12	4	2	0.070	0.429	1	34(2)	CFRS	...
03.0983	0.370	21.03	-19.90	3	5	0.091	0.275	4	0(5)	CFRS	...
03.0992	0.262	22.74	-17.46	2	3	0.149	0.271	4	...	CFRS	...
03.0999	0.704	21.49	-21.39	3	5	0.308	0.233	6	11(2)	CFRS	...
03.1014	0.197	19.32	-20.84	3	5	0.068	0.232	4	6(5)	CFRS	...
03.1016	0.705	22.38	-20.47	3	6	0.145	0.161	6	85(10)	CFRS	...
03.1027	1.038	22.06	-21.64	39	8	0.178	0.239	4	107(7)	CFRS	...
03.1031	0.422	20.62	-20.12	3	2	0.105	0.568	1	0(12)	CFRS	...
03.1032	0.618	20.33	-21.53	4	1	0.110	0.593	1	15(1)	CFRS	...
03.1034	...	22.21	...	0	2	0.057	0.266	1	...	CFRS	...
03.1035	0.635	21.25	-20.84	3	3	0.095	0.435	1	5(2)	CFRS	...
03.1050	0.264	21.49	-18.83	4	4	0.068	0.211	4	67(24)	CFRS	...
03.1051	0.155	21.01	-18.16	4	5	0.045	0.272	4	29(8)	CFRS	...
03.1056	0.944	21.97	-21.23	3	6	0.130	0.303	4	85(2)	CFRS	...
03.1060	0.480	20.72	-20.39	3	3	0.095	0.431	1	6(4)	CFRS	...
03.1077	0.938	21.57	-22.86	3	1	0.143	0.372	4	0(3)	CFRS	...
03.1319	0.620	21.62	-20.61	4	1	0.171	0.425	1	32(7)	CFRS	...
03.1347	0.562	20.60	-21.45	3	3	4	15(2)	CFRS	...
03.1373	0.482	20.73	-20.42	3	3	0.123	0.536	1	0(5)	CFRS	...
03.1375	0.637	22.12	-20.38	3	5	0.130	0.188	6	24(2)	CFRS	...
03.1381	0.636	20.23	-22.02	4	0	0.074	0.551	1	0(5)	CFRS	...
03.1384	0.785	21.61	-21.22	2	1	0.101	0.414	1	54(6)	CFRS	...
03.1387	0.222	20.72	-18.60	1	-1	0.174	0.622	1	...	CFRS	...
03.1392	0.605	20.89	-21.22	4	4	0.070	0.389	1	0(3)	CFRS	...
03.1393	0.852	22.24	-21.21	9	5	0.108	0.220	4	0(3)	CFRS	...
03.1395	0.708	21.79	-20.55	2	3	0.092	0.340	4	7(0)	CFRS	...
03.1413	0.487	20.64	-20.42	2	2	0.091	0.454	1	0(7)	CFRS	...

Table 2—Continued

ID	z	F814W	$M_{B_{AB}}$	Note ^a	Class ^b	A ^c	C ^c	AC-Class ^d	$EW_{[OII]}$ (1σ) ^e	Origin	Old ID ^f
03.1416	0.488	20.22	-21.20	4	1	0.075	0.484	1	2(2)	CFRS	...
03.1426	...	22.00	...	0	6	0.098	0.233	6	...	CFRS	...
03.1499	0.827	21.62	-21.41	93	5	0.071	0.292	4	...	CFRS	...
03.1531	0.715	22.06	-20.70	3	6	0.093	0.134	6	38(5)	CFRS	...
03.1540	0.690	21.04	-21.56	3	4	0.202	0.286	4	18(2)	CFRS	...
03.1650	0.637	21.86	-20.17	3	5	0.092	0.169	6	22(6)	CFRS	...
03.9003	0.619	20.88	-21.16	4	5	0.283	0.201	6	50(2)	CFRS	...
10.0747	0.340	20.40	-20.19	3	4	0.059	0.281	4	...	CFRS	...
10.0761	0.983	22.16	-21.63	3	6	0.061	0.171	4	8(1)	CFRS	...
10.0763	0.671	21.16	-21.85	3	5	0.109	0.232	4	11(2)	CFRS	...
10.0765	0.536	22.35	-19.93	4	6	6	60(6)	CFRS	...
10.0769	0.669	21.17	-21.28	4	2	0.092	0.306	4	4(1)	CFRS	...
10.0771	0.787	22.76	-20.58	8	6	0.116	0.102	6	70(14)	CFRS	...
10.0793	0.577	21.31	-20.86	4	4	0.196	0.289	4	70(9)	CFRS	...
10.0794	0.580	21.16	-20.50	3	1	0.124	0.583	1	0(5)	CFRS	...
10.0802	0.309	21.88	-19.28	4	6	0.293	0.147	6	47(4)	CFRS	...
10.0805	0.147	21.78	-17.44	4	4	0.076	0.164	6	...	CFRS	...
10.0811	0.738	21.37	-21.60	93	4	0.102	0.223	4	...	CFRS	...
10.0812	0.385	20.10	-20.57	4	2	0.048	0.496	1	0(7)	CFRS	...
10.0813	0.467	22.27	-19.45	4	4	0.118	0.210	4	70(14)	CFRS	...
10.0818	0.000	19.23	...	4	-2	-2	...	CFRS	...
10.0826	0.643	20.57	-21.95	3	5	0.135	0.232	4	7(2)	CFRS	...
10.0829	0.526	21.73	-20.24	93	6	0.071	0.212	4	...	CFRS	...
10.1017	0.816	21.66	-21.50	2	4	0.058	0.195	4	0(4)	CFRS	...
10.1153	0.552	21.03	-20.64	4	4	0.099	0.308	4	0(3)	CFRS	...
10.1155	0.507	21.13	-20.89	4	5	0.206	0.346	4	123(13)	CFRS	...
10.1161	0.200	20.03	-18.91	4	2	0.074	0.457	1	5(2)	CFRS	...
10.1178	0.197	21.63	-17.94	4	4	0.127	0.217	4	...	CFRS	...
10.1180	0.465	20.19	-21.15	3	3	0.046	0.402	1	0(1)	CFRS	...
10.1182	0.471	22.26	-19.38	3	6	0.086	0.204	4	48(18)	CFRS	...
10.1183	0.649	20.60	-21.92	4	3	0.156	0.277	4	57(16)	CFRS	...
10.1189	0.949	21.71	-21.98	2	3	0.163	0.351	4	0(5)	CFRS	...
10.1203	0.686	22.28	-20.29	3	6	0.129	0.255	4	62(2)	CFRS	...
10.1207	0.706	21.42	-20.64	3	1	0.155	0.367	4	48(16)	CFRS	...
10.1209	0.841	21.32	-21.97	3	1	0.107	0.499	1	0(7)	CFRS	...
10.1213	0.817	21.95	-21.04	3	6	0.072	0.175	4	27(2)	CFRS	...
10.1220	0.909	22.28	-21.10	3	6	0.394	0.357	4	38(4)	CFRS	...
10.1222	0.519	21.42	-20.15	3	4	0.180	0.287	4	25(16)	CFRS	...
10.1231	0.473	21.09	-20.07	3	1	0.067	0.464	1	46(13)	CFRS	...
10.1233	...	21.45	...	0	5	0.078	0.221	4	...	CFRS	...
10.1236	0.750	22.12	-20.91	3	4	0.215	0.226	6	14(4)	CFRS	...
10.1243	0.585	20.92	-20.84	3	3	0.055	0.449	1	0(10)	CFRS	...
10.1255	0.467	19.41	-21.95	4	0	0.045	0.475	1	9(6)	CFRS	...
10.1257	0.777	21.42	-21.29	3	4	0.023	0.375	1	0(4)	CFRS	...
10.1262	0.578	21.65	-20.20	3	1	0.116	0.438	1	0(5)	CFRS	...
10.1270	0.670	21.26	-21.08	4	4	0.071	0.423	1	...	CFRS	...
10.1281	0.111	21.80	-15.79	3	6	0.119	0.210	4	...	CFRS	...
10.1313	...	22.37	...	0	0	0.122	0.319	1	...	CFRS	...
10.1349	0.468	20.56	-20.91	4	3	0.081	0.356	4	13(5)	CFRS	...
10.1423	0.724	22.59	-20.23	2	1	0.100	0.465	1	14(3)	CFRS	...
10.1502	...	22.04	...	0	4	0.099	0.407	4	...	CFRS	...
10.1612	0.073	21.18	-15.92	3	5	0.077	0.189	4	...	CFRS	...

Table 2—Continued

ID	z	F814W	$M_{B_{AB}}$	Note ^a	Class ^b	A ^c	C ^c	AC-Class ^d	$EW_{[OII]}$ (1σ) ^e	Origin	Old ID ^f
10.1613	0.076	21.33	-16.11	1	6	0.117	0.205	4	...	CFRS	...
10.1614	0.000	18.46	...	4	-2	-2	...	CFRS	...
10.1631	0.000	20.14	...	4	-2	-2	...	CFRS	...
10.1637	0.497	20.56	-20.79	4	1	0.085	0.519	1	0(6)	CFRS	...
10.1643	0.234	20.61	-18.90	4	4	0.146	0.354	4	...	CFRS	...
10.1644	0.077	19.90	-17.09	4	6	0.066	0.259	4	...	CFRS	...
10.1650	0.007	19.21	-14.88	4	6	0.353	0.199	6	...	CFRS	...
10.1651	0.197	20.28	-18.53	4	2	0.093	0.502	1	...	CFRS	...
14.0147	1.181	22.26	-21.76	9	6	0.122	0.158	6	...	CFRS	...
14.0163	0.000	18.99	...	4	-2	-2	...	CFRS	...
14.0198	1.603	20.06	...	14	-1	0.159	0.847	-1	...	CFRS	...
14.0207	0.546	19.67	-22.19	4	2	0.056	0.612	1	0(15)	CFRS	...
14.0293	0.761	21.25	-21.82	3	4	0.082	0.312	4	12(0)	GRTH	...
14.0310	0.238	20.93	-19.40	4	6	0.054	0.236	4	36(0)	CFRS	...
14.0312	0.746	21.80	-20.86	3	4	0.161	0.268	4	19(0)	GRTH	...
14.0377	0.260	20.81	-19.61	4	6	0.218	0.130	6	79(30)	CFRS	...
14.0384	0.000	21.97	...	2	-2	-2	...	CFRS	...
14.0393	0.602	20.49	-21.93	4	5	0.205	0.147	4	22(1)	CFRS	...
14.0400	0.674	21.38	-21.19	4	4	0.089	0.284	4	12(0)	GRTH	...
14.0411	0.836	21.45	-21.65	3	6	0.212	0.399	1	57(0)	GRTH	...
14.0422	0.421	20.39	-20.64	2	1	0.073	0.479	1	3(1)	CFRS	...
14.0435	0.068	18.39	-18.83	3	3	0.051	0.454	1	...	CFRS	...
14.0443	0.000	20.14	...	4	-2	-2	...	CFRS	...
14.0462	0.000	22.22	...	3	-2	-2	...	CFRS	...
14.0485	0.654	22.20	-20.47	3	4	0.037	0.238	4	34(5)	CFRS	...
14.0501	0.372	21.66	-20.00	4	6	0.077	0.205	4	44(0)	GRTH	...
14.0516	...	22.22	...	0	1	0.116	0.432	1	...	GRTH	...
14.0528	0.064	20.61	-16.89	4	1	0.107	0.479	1	...	CFRS	...
14.0529	0.000	18.45	...	4	-2	-2	...	CFRS	...
14.0547	1.160	21.40	-23.09	3	6	0.223	0.115	6	13(0)	GRTH	...
14.0574	0.000	21.66	...	2	-2	-2	...	CFRS	...
14.0593	0.614	22.48	-20.41	3	6	0.163	0.176	6	29(4)	CFRS	...
14.0608	0.969	22.16	-21.43	2	6	0.118	0.180	6	10(0)	GRTH	...
14.0620	0.000	22.25	...	3	-2	-2	...	CFRS	...
14.0651	0.637	22.02	-20.30	1	2	0.066	0.437	1	...	CFRS	...
14.0665	0.809	22.97	-20.78	2	6	6	22(0)	GRTH	...
14.0666	0.000	21.31	...	4	-2	-2	...	CFRS	...
14.0685	0.081	17.85	-19.96	4	2	0.065	0.524	1	...	CFRS	...
14.0695	0.266	21.39	-19.08	4	1	0.131	0.347	4	40(0)	GRTH	...
14.0700	0.643	20.42	-21.60	4	2	0.082	0.590	1	0(0)	GRTH	...
14.0725	0.582	22.11	-19.74	3	6	0.190	0.230	4	42(3)	CFRS	...
14.0743	0.986	22.19	-22.05	2	6	0.105	0.182	6	28(0)	GRTH	...
14.0746	0.675	21.43	-20.68	3	2	0.068	0.423	1	0(5)	CFRS	...
14.0749	0.818	22.41	-20.61	2	6	0.126	0.185	6	18(0)	GRTH	...
14.0760	...	22.07	...	0	8	6	...	CFRS	...
14.0807	0.985	21.88	-21.82	2	3	0.088	0.344	4	9(0)	GRTH	...
14.0846	0.989	21.81	-21.91	92	6	0.313	0.193	6	...	CFRS	...
14.0848	0.662	22.60	-20.31	3	3	0.136	0.263	4	37(9)	CFRS	...
14.0851	...	21.99	...	0	2	0.121	0.293	1	...	CFRS	...
14.0854	0.992	21.63	-22.31	2	1	0.096	0.423	1	0(5)	CFRS	...
14.0899	0.875	21.71	-21.73	9	3	0.054	0.288	4	9(2)	CFRS	...
14.0916	0.325	20.95	-19.94	3	3	0.085	0.328	4	18(3)	CFRS	...

Table 2—Continued

ID	z	F814W	$M_{B_{AB}}$	Note ^a	Class ^b	A ^c	C ^c	AC-Class ^d	$EW_{[OII]}$ (1σ) ^e	Origin	Old ID ^f
14.0922	0.000	22.29	...	4	-2	-2	...	CFRS	...
14.0939	0.918	21.96	-22.24	1	6	0.268	0.340	4	0(0)	GRTH	...
14.0972	0.674	21.15	-21.53	4	6	0.148	0.378	4	66(1)	CFRS	...
14.0983	0.286	21.26	-19.59	4	3	0.103	0.373	4	34(0)	GRTH	...
14.0985	0.807	22.29	-20.62	3	4	0.094	0.204	4	27(5)	CFRS	...
14.1008	0.433	20.66	-20.51	3	4	0.090	0.397	1	9(0)	GRTH	...
14.1012	0.479	21.46	-20.41	3	1	0.054	0.381	1	29(2)	CFRS	...
14.1028	0.988	21.63	-22.22	3	2	0.159	0.415	1	31(3)	CFRS	...
14.1037	0.549	21.27	-20.63	3	6	0.099	0.223	4	24(3)	CFRS	...
14.1039	0.079	19.57	-18.51	4	6	0.153	0.423	1	...	CFRS	...
14.1042	0.722	21.33	-21.07	3	2	0.137	0.480	1	13(1)	CFRS	...
14.1043	0.641	20.22	-22.20	4	3	0.043	0.404	1	0(3)	CFRS	...
14.1052	0.000	17.58	...	4	-2	-2	...	CFRS	...
14.1071	0.359	22.32	-18.67	3	4	0.199	0.094	6	57(12)	CFRS	...
14.1079	0.901	21.82	-21.45	9	6	0.086	0.284	4	38(3)	CFRS	...
14.1087	0.659	21.95	-20.58	3	8	0.137	0.134	6	52(4)	CFRS	...
14.1103	0.209	22.41	-17.75	4	-1	0.124	0.564	1	0(17)	CFRS	...
14.1126	0.743	22.20	-20.72	3	6	0.154	0.164	6	62(6)	CFRS	...
14.1129	0.831	21.12	-22.10	3	6	0.251	0.115	6	28(0)	GRTH	...
14.1136	0.640	22.02	-20.98	3	8	0.131	0.346	4	73(5)	CFRS	...
14.1139	0.660	20.48	-22.31	3	6	0.159	0.227	4	16(1)	CFRS	...
14.1143	0.673	22.44	-20.10	93	3	0.063	0.256	4	...	CFRS	...
14.1146	0.744	21.68	-21.12	3	8	0.185	0.274	4	53(4)	CFRS	...
14.1158	0.000	20.81	...	3	-2	-2	...	CFRS	...
14.1164	0.671	21.76	-20.94	3	6	0.120	0.211	4	34(0)	GRTH	...
14.1166	1.015	22.28	-21.36	3	1	0.089	0.358	4	56(6)	CFRS	...
14.1178	...	22.22	...	0	1	0.101	0.326	1	...	GRTH	...
14.1179	0.434	21.44	-19.73	2	2	0.142	0.483	1	0(14)	CFRS	...
14.1189	0.753	22.06	-20.80	3	4	0.152	0.302	4	43(6)	CFRS	...
14.1190	0.754	21.06	-21.84	3	3	0.102	0.276	4	9(2)	CFRS	...
14.1193	0.078	21.67	-16.61	4	6	0.220	0.179	6	...	CFRS	...
14.1200	0.235	21.84	-18.21	2	6	0.096	0.163	6	0(42)	CFRS	...
14.1209	0.234	20.98	-19.43	4	3	0.045	0.283	4	...	CFRS	...
14.1234	0.000	22.16	...	4	-2	-2	...	CFRS	...
14.1239	0.362	21.74	-19.68	3	6	0.099	0.220	4	47(2)	CFRS	...
14.1242	0.290	21.69	-19.03	3	6	0.339	0.099	6	33(25)	CFRS	...
14.1251	0.814	22.17	-20.42	3	4	0.076	0.411	1	0(0)	GRTH	...
14.1257	0.291	20.68	-19.82	3	4	0.066	0.248	4	55(0)	GRTH	...
14.1258	0.645	22.39	-20.25	3	1	0.116	0.323	4	62(9)	CFRS	...
14.1264	0.703	22.80	-20.00	91	8	6	...	CFRS	...
14.1273	0.257	21.94	-18.64	4	6	0.111	0.217	4	57(33)	CFRS	...
14.1277	0.810	21.33	-21.93	2	8	0.131	0.387	1	19(10)	CFRS	...
14.1281	0.141	21.07	-18.07	3	3	0.091	0.390	1	30(0)	GRTH	...
14.1311	0.806	20.58	-22.90	3	1	0.087	0.442	1	0(1)	CFRS	...
14.1321	0.106	21.40	-17.39	4	8	0.107	0.278	4	...	CFRS	...
14.1356	0.831	22.23	-21.10	3	8	0.081	0.199	6	47(7)	CFRS	...
14.1371	0.000	18.70	...	3	-2	-2	...	CFRS	...
14.1395	0.530	21.78	-20.20	4	4	0.134	0.210	4	63(8)	CFRS	...
14.1415	0.745	21.06	-21.62	2	1	0.138	0.445	1	0(0)	GRTH	...
14.1419	0.236	22.72	-16.21	93	-1	0.195	0.374	4	...	CFRS	...
14.1427	0.860	21.54	-21.50	9	4	0.114	0.278	4	33(0)	GRTH	...
14.1446	0.348	20.07	-21.10	4	1	0.058	0.468	1	24(1)	CFRS	...

Table 2—Continued

ID	z	F814W	$M_{B_{AB}}$	Note ^a	Class ^b	A ^c	C ^c	AC-Class ^d	$EW_{[OII]}$ (1σ) ^e	Origin	Old ID ^f
14.1464	0.462	21.06	-19.94	2	0	0.171	0.514	1	11(8)	CFRS	...
14.1496	0.899	21.93	-21.61	3	-1	0.105	0.405	1	54(6)	CFRS	...
14.1501	0.989	22.02	-21.98	2	6	0.241	0.187	6	60(0)	GRTH	...
14.1502	...	22.26	...	0	3	0.087	0.260	4	...	GRTH	...
14.1524	0.427	19.87	-21.89	3	3	0.124	0.243	4	15(0)	GRTH	...
14.9025	0.155	19.16	-20.28	4	3	0.084	0.453	1	...	CFRS	...
14.9987	0.420	22.48	-18.86	92	4	0.110	0.373	4	25(0)	CFRS	...
22.0377	...	22.28	...	0	3	0.077	0.327	4	...	CFRS	...
22.0434	0.094	19.90	-18.83	4	5	0.062	0.268	4	...	CFRS	...
22.0453	0.623	22.12	-20.25	3	6	0.150	0.234	4	...	CFRS	...
22.0497	0.470	19.42	-22.75	4	0	0.171	0.369	4	0(5)	CFRS	...
22.0501	0.424	20.48	-20.77	4	0	0.053	0.436	1	0(9)	CFRS	...
22.0541	...	22.69	...	0	3	0.099	0.217	4	...	CFRS	...
22.0576	0.890	21.93	-21.12	9	6	0.225	0.445	1	63(25)	CFRS	...
22.0583	0.431	21.63	-19.36	3	5	0.075	0.189	4	36(21)	CFRS	...
22.0585	0.294	20.74	-19.40	2	2	0.155	0.348	4	0(24)	CFRS	...
22.0599	0.889	21.62	-21.66	9	6	0.092	0.330	4	64(11)	CFRS	...
22.0609	0.475	20.60	-20.84	3	3	0.085	0.357	4	0(11)	CFRS	...
22.0618	0.830	22.28	-20.78	1	2	0.054	0.333	4	...	CFRS	...
22.0622	0.325	21.92	-18.58	3	4	0.211	0.401	1	13(8)	CFRS	...
22.0671	0.319	20.87	-20.24	4	3	0.115	0.371	4	31(5)	CFRS	...
22.0676	0.141	20.69	-18.24	4	2	0.063	0.422	1	...	CFRS	...
22.0758	0.294	19.54	-20.80	3	0	0.050	0.491	1	0(5)	CFRS	...
22.0764	0.819	21.98	-20.91	3	6	0.128	0.148	6	19(3)	CFRS	...
22.0779	0.925	21.89	-21.64	9	3	0.169	0.370	4	12(2)	CFRS	...
22.0819	0.293	20.86	-19.61	4	4	0.087	0.239	4	45(3)	CFRS	...
22.0890	...	21.28	...	0	2	0.088	0.399	1	...	CFRS	...
22.0919	0.474	21.29	-20.25	4	6	0.320	0.487	1	8(1)	CFRS	...
22.0923	...	22.28	...	0	4	0.149	0.182	4	...	CFRS	...
22.0944	0.249	18.84	-21.59	3	4	0.061	0.388	1	0(57)	CFRS	...
22.0945	0.676	21.93	-20.71	3	5	0.164	0.186	6	17(3)	CFRS	...
22.0953	0.977	22.33	-21.39	8	6	0.084	0.154	6	34(6)	CFRS	...
22.0988	0.477	22.83	-19.13	93	5	0.157	0.116	6	...	CFRS	...
22.1015	0.231	23.38	-15.50	94	3	4	...	CFRS	...
22.1037	0.550	21.91	-19.91	2	2	0.218	0.471	1	163(29)	CFRS	...
22.1078	0.671	22.13	-20.65	1	1	0.241	0.477	1	...	CFRS	...
22.1279	0.594	21.28	-20.70	3	1	0.089	0.358	1	0(20)	CFRS	...
22.1313	0.819	22.24	-21.45	3	6	0.154	0.131	6	73(5)	CFRS	...
22.1374	0.093	18.21	-20.45	4	4	0.054	0.334	4	...	CFRS	...
22.1406	0.818	21.97	-20.97	4	-1	0.121	0.319	4	100(4)	CFRS	...
22.1453	0.816	21.61	-21.59	3	6	0.340	0.163	6	0(3)	CFRS	...
22.1466	...	21.85	...	0	3	0.135	0.273	4	...	CFRS	...
22.1486	0.953	22.58	-21.32	8	-1	-1	12(6)	CFRS	...
22.1507	0.820	21.37	-21.48	3	1	0.098	0.446	1	0(2)	CFRS	...
10.10116	...	19.75	...	0	4	0.085	0.332	4	...	Autofib	10f_14
10.11699	0.000	19.76	...	4	-2	-2	...	LDSS1	10.2.9HI
10.11702	0.168	19.36	...	4	2	0.118	0.511	1	10(-9)	LDSS1	10.2.12HI
10.11703	0.437	19.63	...	4	3	0.050	0.429	1	5(-9)	LDSS1	10.2.13HI
10.11706	0.151	21.27	...	4	6	0.230	0.133	6	21(-9)	LDSS1	10.2.16HI
10.11709	0.179	20.94	...	4	3	0.046	0.276	4	16(-9)	LDSS1	10.2.19HI
10.12058	...	23.36	...	0	6	0.268	0.081	6	...	LDSS2	10.21.227
10.12059	0.307	21.15	...	4	5	0.049	0.218	4	20(2)	LDSS2	10.21.233

Table 2—Continued

ID	z	F814W	$M_{B_{AB}}$	Note ^a	Class ^b	A ^c	C ^c	AC-Class ^d	$EW_{[OII]}$ (1σ) ^e	Origin	Old ID ^f
10.12060	0.294	21.23	-18.39	4	1	0.120	0.493	1	12(4)	LDSS2	10.21.262
10.12062	0.634	21.85	-20.21	4	0	0.110	0.475	1	55(1)	LDSS2	10.21.279
10.12063	1.108	22.27	-21.36	4	-1	0.161	0.397	1	65(10)	LDSS2	10.21.288
10.12065	0.207	20.97	-17.85	4	1	0.103	0.587	1	19(6)	LDSS2	10.21.328
10.12066	0.924	22.30	-20.36	2	6	0.104	0.155	6	17(8)	LDSS2	10.21.22
10.12071	0.177	21.25	-17.84	4	3	0.082	0.283	4	0(8)	LDSS2	10.21.88
10.12073	0.492	20.35	-20.61	4	6	0.074	0.354	4	0(0)	LDSS2	10.21.109
10.12076	0.323	21.91	-18.40	4	5	0.067	0.208	4	25(5)	LDSS2	10.21.301
10.12078	0.296	22.82	...	4	3	0.072	0.196	4	58(8)	LDSS2	10.22.223
10.12080	0.314	20.81	-18.96	4	-1	0.182	0.643	1	0(3)	LDSS2	10.22.248
10.12081	0.563	22.23	-19.42	4	6	0.221	0.142	6	17(2)	LDSS2	10.22.260
10.12085	...	23.02	...	0	6	0.259	0.109	6	...	LDSS2	10.22.315
10.12086	0.324	22.13	-18.24	4	6	0.105	0.159	6	50(3)	LDSS2	10.22.330
10.12087	2.749	22.81	...	4	-1	-1	...	LDSS2	10.22.25
10.12089	0.384	20.39	-19.99	4	1	0.060	0.500	1	0(3)	LDSS2	10.22.61
10.12091	0.476	20.25	-20.76	4	3	0.104	0.456	1	10(2)	LDSS2	10.22.71
10.12092	0.436	20.23	...	4	2	0.090	0.490	1	0(2)	LDSS2	10.22.77
10.12095	0.724	21.75	-20.59	2	6	0.073	0.218	4	30(2)	LDSS2	10.22.122
10.12519	0.097	19.74	-18.45 ^h	4	3	0.182	0.315	4	0(0)	LDSS2	10.23.218
10.12520	1.999	22.42	...	4	-1	-1	...	LDSS2	10.23.222
10.12522	0.000	19.02	...	4	-2	-2	...	LDSS2	10.23.235
10.12524	0.149	21.51	-17.16	4	2	0.108	0.326	4	42(5)	LDSS2	10.23.255
10.12525	0.435	19.79	-20.81	4	1	0.291	0.069	1	3(1)	LDSS2	10.23.273
10.12527	0.000	19.87	...	4	-2	-2	...	LDSS2	10.23.332
10.12528	0.582	20.69	-21.11	4	5	0.088	0.317	4	8(1)	LDSS2	10.23.28
10.12529	...	23.16	...	0	6	0.243	0.163	6	...	LDSS2	10.23.32
10.12530	0.476	20.50	-20.42	4	3	0.123	0.468	1	0(0)	LDSS2	10.23.40
10.12534	...	21.31	...	0	-1	0.238	0.549	-1	...	LDSS2	10.23.92
10.12535	0.000	18.07	...	4	-2	-2	...	LDSS2	10.23.105
10.12536	1.256	21.00	...	4	-1	0.158	0.622	1	...	LDSS2	10.23.116
10.12537	0.000	21.69	...	4	-2	-1	...	LDSS2	10.23.126
10.12786	...	21.88	...	0	6	6	...	LDSS1	10.2.2FB
10.12787	0.283	22.32	...	4	-1	-1	...	LDSS1	10.2.5FB
13.10222	0.052	18.98	-17.23 ⁱ	-1	3	0.059	0.249	4	0(-9)	Autofib	13b_14
13.10379	...	19.35	...	0	-2	-2	...	Autofib	13m_16
13.11753	0.198	19.08	...	2	4	4	28(-9)	LDSS1	13.2.1HI
13.11772	0.512	20.90	...	4	4	0.098	0.353	4	63(-9)	LDSS1	13.2.20HI
13.11874	...	19.33	...	0	3	0.064	0.415	4	...	Autofib	13f1_1
13.11924	0.281	18.86	-19.83 ⁱ	-1	1	0.085	0.634	1	0(-9)	Autofib	13f1_63
13.11925	0.256	20.34	-18.83 ⁱ	-1	3	0.061	0.320	4	46(-9)	Autofib	13f1_64
13.11976	0.336	21.37	-18.93 ⁱ	-1	5	0.090	0.247	4	100(-9)	Autofib	13xf_64
13.12099	0.385	21.00	-19.69	4	5	0.095	0.345	4	19(2)	LDSS2	13.21.323
13.12106	0.556	21.60	-20.09	4	6	0.103	0.200	4	14(3)	LDSS2	13.21.465
13.12107	0.556	21.22	-20.47	2	2	0.143	0.389	1	34(5)	LDSS2	13.21.480
13.12109	0.462	22.25	-18.97	2	5	0.153	0.143	4	36(7)	LDSS2	13.21.517
13.12111	0.089	22.31	-15.42	4	6	0.191	0.154	6	41(7)	LDSS2	13.21.27
13.12112	0.424	21.09	-19.92	4	2	0.102	0.474	1	12(2)	LDSS2	13.21.38
13.12116	0.187	21.18	-17.94	4	1	0.058	0.472	1	59(14)	LDSS2	13.21.106
13.12117	0.536	22.05	-19.55	2	5	0.094	0.224	4	32(3)	LDSS2	13.21.123
13.12118	0.335	21.86	-18.61	4	5	0.135	0.333	4	35(4)	LDSS2	13.21.160
13.12538	...	21.71	...	0	2	0.085	0.490	1	...	LDSS2	13.21.311
13.12539	0.000	19.97	...	4	-2	-2	...	LDSS2	13.22.325

Table 2—Continued

ID	z	F814W	$M_{B_{AB}}$	Note ^a	Class ^b	A ^c	C ^c	AC-Class ^d	$EW_{[OII]}$ (1 σ) ^e	Origin	Old ID ^f
13.12540	0.452	22.33	-18.99	2	6	0.148	0.178	6	0(0)	LDSS2	13.22.344
13.12542	...	22.03	...	0	6	0.200	0.153	6	...	LDSS2	13.22.367
13.12545	0.830	20.14	-22.57	4	6	0.195	0.289	4	19(1)	LDSS2	13.22.400
13.12546	0.283	20.01	-19.44	4	3	0.112	0.528	1	0(0)	LDSS2	13.22.417
13.12549	0.493	21.02	-20.26	4	3	0.105	0.328	4	13(1)	LDSS2	13.22.469
13.12550	0.000	18.44	...	4	-2	-2	...	LDSS2	13.22.484
13.12551	...	22.12	...	0	5	0.077	0.224	4	...	LDSS2	13.22.492
13.12552	0.566	20.42	-21.14	4	3	0.093	0.268	4	7(1)	LDSS2	13.22.510
13.12553	0.278	20.47	-19.42	4	3	0.086	0.310	4	8(3)	LDSS2	13.22.519
13.12554	...	20.90	...	0	4	0.318	0.233	4	...	LDSS2	13.22.12
13.12555	0.426	21.99	-19.09	2	-1	0.165	0.385	1	4(0)	LDSS2	13.22.28
13.12556	...	22.57	...	0	-2	-2	...	LDSS2	13.22.34
13.12559	...	22.73	...	0	-1	-1	...	LDSS2	13.22.98
13.12560	0.363	20.49	-19.90	4	1	0.067	0.528	1	7(2)	LDSS2	13.22.116
13.12561	0.326	19.51	-20.73	4	3	0.106	0.519	1	4(1)	LDSS2	13.22.131
13.12566	0.000	19.59	...	4	-2	-2	...	LDSS2	13.22.180
13.12567	...	22.28	...	0	1	0.152	0.422	1	...	LDSS2	13.22.186
13.12759	0.000	21.07	...	4	-2	-2	...	LDSS1	13.2.9LO
13.12764	...	21.97	...	0	2	0.156	0.457	1	...	LDSS1	13.2.14LO
13.12767	...	21.84	...	0	-1	-1	...	LDSS1	13.2.17LO
13.12783	...	22.45	...	0	8	0.210	0.205	6	...	LDSS1	13.2.35LO
13.12795	2.934	21.85	...	4	-1	-1	...	LDSS1	13.2.1FB
13.12797	0.627	22.69	...	2	-1	-1	...	LDSS1	13.2.3FB
13.12798	0.297	22.78	...	2	-1	-1	...	LDSS1	13.2.4FB
13.12801	...	22.47	...	0	6	0.157	0.167	6	...	LDSS1	13.2.7FB
13.12802	0.667	22.63	...	2	2	0.120	0.233	4	...	LDSS1	13.2.9FB
13.12803	...	23.10	...	0	6	6	...	LDSS1	13.2.11FB
13.12808	0.000	22.18	...	0	-2	-2	...	LDSS1	13.2.28LO
13.12810	...	22.30	...	0	-1	-1	...	LDSS1	13.2.10FB
13.12811	0.550	21.90	...	2	4	0.137	0.193	4	...	LDSS1	13.2.13FB

^aThe confidence class for the redshift. For the LDSS objects this has been transformed to the CFRS system by assigning note=4 to confident redshifts, note=2 to less secure redshifts and 0 for failures. For the few LDSS objects for which there is no confidence class, we have assigned note=-1

^bThe eyeball classification for the object

^cThe A&C parameters (uncorrected), see Section 3.2

^dThe AC classification for the object using the division lines in Figure 8

^eThe equivalent width of [OII]. For the CFRS objects this is from Hammer et al. (1997), for the LDSS objects from the Autofib survey (Ellis et al. 1996).

^fThe identification given in the original LDSS paper

^gThe object is clearly extended, but was given $z = 0$ in in the CFRS survey.

^hThe HST photometry here is uncertain and $M_{B_{AB}}$ is based on the original b_J photometry.

ⁱThe absolute magnitude is the original Autofib absolute magnitude based on b_J transformed to AB.

Table 3. HST Survey Completeness

Survey	Survey limits	Completeness		Effective area ^a deg ²
		Geometric	Spectroscopic	
CFRS	$17.5 < I_{AB} < 22.5$	0.5477	90.44%	0.01377
LDSS-2 (10hr)	$22.5 < b_J < 24.0$	0.7941	85.19%	0.002513
LDSS-2 (13hr) ^b	$22.5 < b_J < 23.3$	0.4516	85.71%	0.001576

^aDefined as surveyed area times the geometric completeness

^bThe LDSS-2 13hr field have less deep spectroscopy, we have adopted the completeness limits as discussed in Glazebrook et al. (1995b)

Table 4. The movement of Frei galaxies in the AC plane

	AC-E	AC-S	AC-P	\mathcal{D}_{SP}^b	\mathcal{D}_{PS}^b	\mathcal{D}_{SE}^b	\mathcal{D}_{ES}^b
Drift coefficients for corrections to R rest frame morphologies							
z=0.0 ^a	33	41	5	0	0	0	0
z=0.2	29	30	6	0	0	0.06 ± 0.04	0
z=0.7	30	29	5	0.13 ± 0.09	0	0.20 ± 0.12	0.32 ± 0.13
z=0.9	16	22	6	0.24 ± 0.11	0	0.10 ± 0.07	0.33 ± 0.12
Drift coefficients for corrections to B_J rest frame morphologies							
z=0.0 ^a	33	41	5	0	0.67 ± 0.21	0.29 ± 0.08	0.05 ± 0.05
z=0.2	29	30	6	0	0.67 ± 0.24	0.35 ± 0.10	0
z=0.7	30	29	5	0.05 ± 0.05	0.67 ± 0.47	0.43 ± 0.14	0.30 ± 0.17
z=0.9	16	22	6	0.07 ± 0.05	0.20 ± 0.20	0.26 ± 0.10	0.21 ± 0.12

^aThe numbers for $z = 0$ are for all Frei galaxies.

^bThe errors are 1σ Poisson errors.

Table 5. Adopted local LF ($H_0 = 50$ km/s/Mpc)

Hubble type	$M^* (b_J)$	α	$\phi^*(Mpc^{-3})$
E/S0	−21.21	−1.00	1.39×10^{-3}
Sab	−20.90	−1.00	6.0×10^{-4}
Sbc	−20.90	−1.00	1.1×10^{-3}
Scd	−20.90	−1.00	4.5×10^{-4}
Sdm	−20.90	−1.00	2.6×10^{-4}
Irr	−20.29	−1.87	7.5×10^{-5}

Fig. 1.— The absolute magnitude - redshift distribution for the combined CFRS and LDSS-2 surveys (assuming $H_0=50$ kms s^{-1} Mpc $^{-1}$). Open symbols refer to the CFRS sample limited at $I(AB)=22.5$; filled symbols refer to the LDSS-2 survey limited at $b_J=24$. The objects in the HST survey are indicated with circles.

Fig. 2.— The relative contributions of the LDSS-2 and CFRS redshift surveys to the total redshift distribution for the sample used in the analysis.

Fig. 3.— Verifying the absolute magnitude scales of the CFRS and LDSS-2 redshift surveys. Top panel: $B_{AB} - b_J$ colour for the LDSS-2 galaxies. Middle panel: Difference in M_B for CFRS galaxies using the CFRS and LDSS-2 SEDs. Bottom panel: The redshift dependence of M_B differences obtained by calculating k -corrections for the LDSS-2 galaxies using b_J and I_{F814W} .

Fig. 4.— Examples of the morphological types used in this paper, with the total number of objects in each class in the survey. Each image is 6×6 arcsec 2 .

Fig. 5.— Correlation between the different classifiers. The radii of the circles are proportional to the value in the correlation matrix. The correlation between the different classifiers is only slightly larger than the internal scatter of one classifier.

Fig. 6.— The distribution of galaxies in the $M(B_{AB}) - z$ plane for the HST survey. Inlaid histograms show the fractional contribution of the four different visual classes as a function of redshift. In this plot the tadpoles have been grouped with the irregular galaxies.

Fig. 7.— Number magnitude counts for the survey (filled circles) compared with those from the larger MDS survey (open triangles). Error bars are Poissonian (Gehrels 1986). In this plot the tadpoles have been grouped with the irregulars.

Fig. 8.— Upper panel: The distribution of galaxies in the $A - C$ plane. Only objects with area larger than 64 contiguous pixels are shown. Bottom panel: The classification angle Θ (see text) plotted versus the eyeball classification for each object. The large circles show the median of each eyeball class.

Fig. 9.— The absolute magnitude distribution of the Frei *et al* galaxies with the selection limits appropriate for the deep HST survey overlaid. The selection function for Sbc galaxies is indicated.

Fig. 10.— Top panel: The change in asymmetry A between the R and B_J images of the local Frei *et al* galaxies. Filled circles denote late type systems for which the trends are somewhat more pronounced. Bottom Panel: as above for the concentration C illustrating the effect of the bandshifting effects on A&C classifications. Labelled lines define the boundary where the change in C would move an object to a different class as indicated (assuming A is at the median of the distribution)

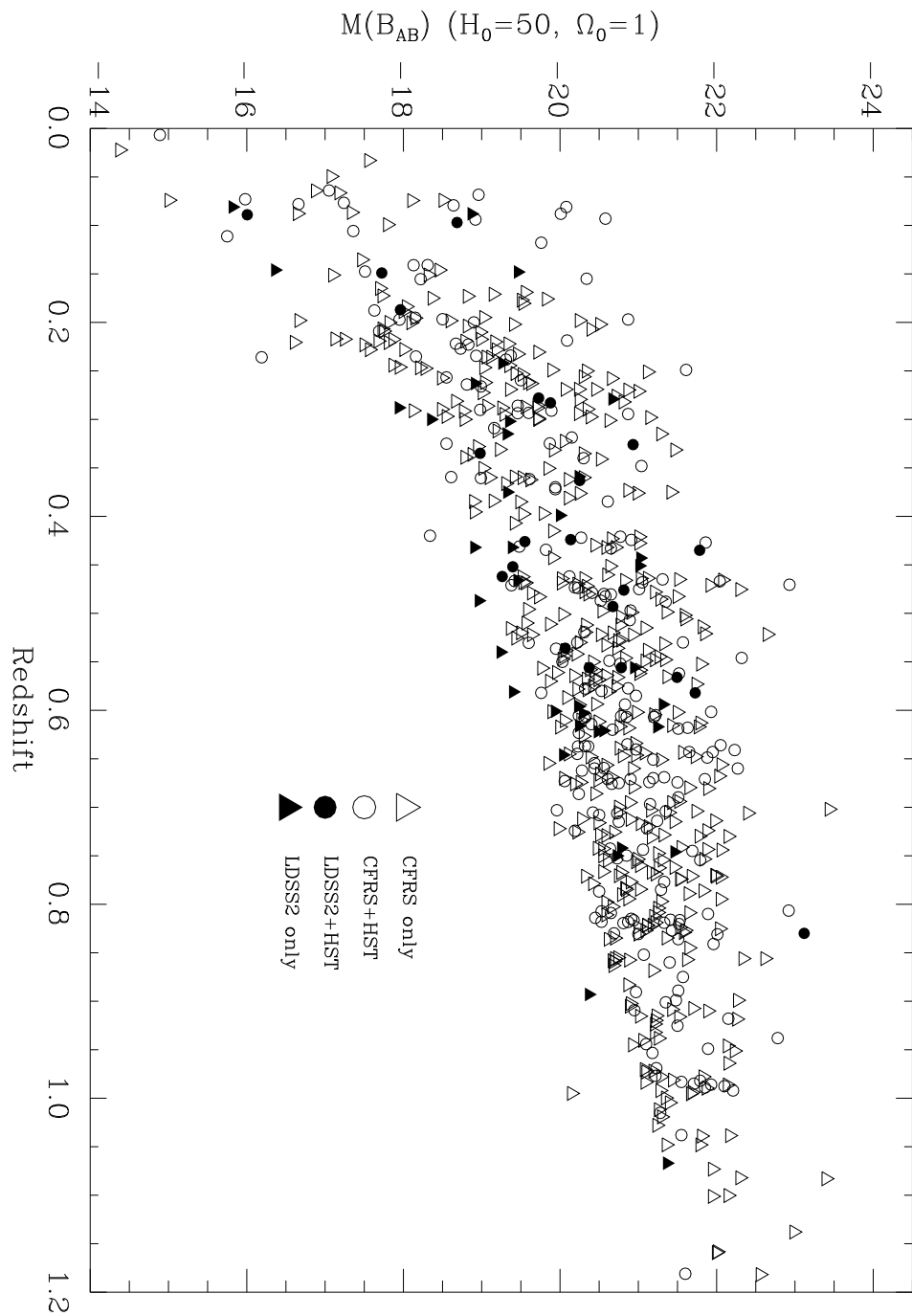
Fig. 11.— The objects classed as *AC*-peculiar sorted by increasing redshift upwards the page. The left column contains objects with $\text{EW}[\text{OII}] = 0$ or unknown. The galaxies in the middle column have $0 < \text{EW}[\text{OII}] < 40$ and the right galaxies the objects with $\text{EW}[\text{OII}] > 40$. Every image is $6 \times 6 \text{ arcsec}^2$, with the exception of 10.1650 which is $12 \times 12 \text{ arcsec}^2$.

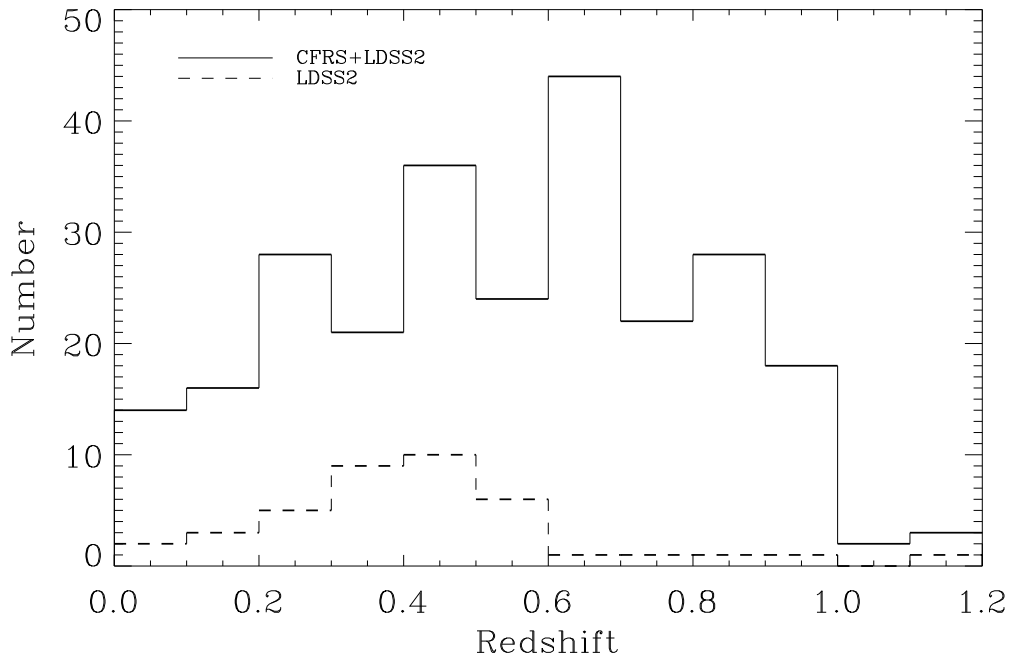
Fig. 12.— Redshift distribution of the three broad *AC* classes compared with theoretical predictions for no-evolution (dashed line) and for mild evolution corresponding to one magnitude of luminosity evolution at $z = 1$ (dash-dotted line). The models have been corrected to observed numbers using the method outlined in the text.

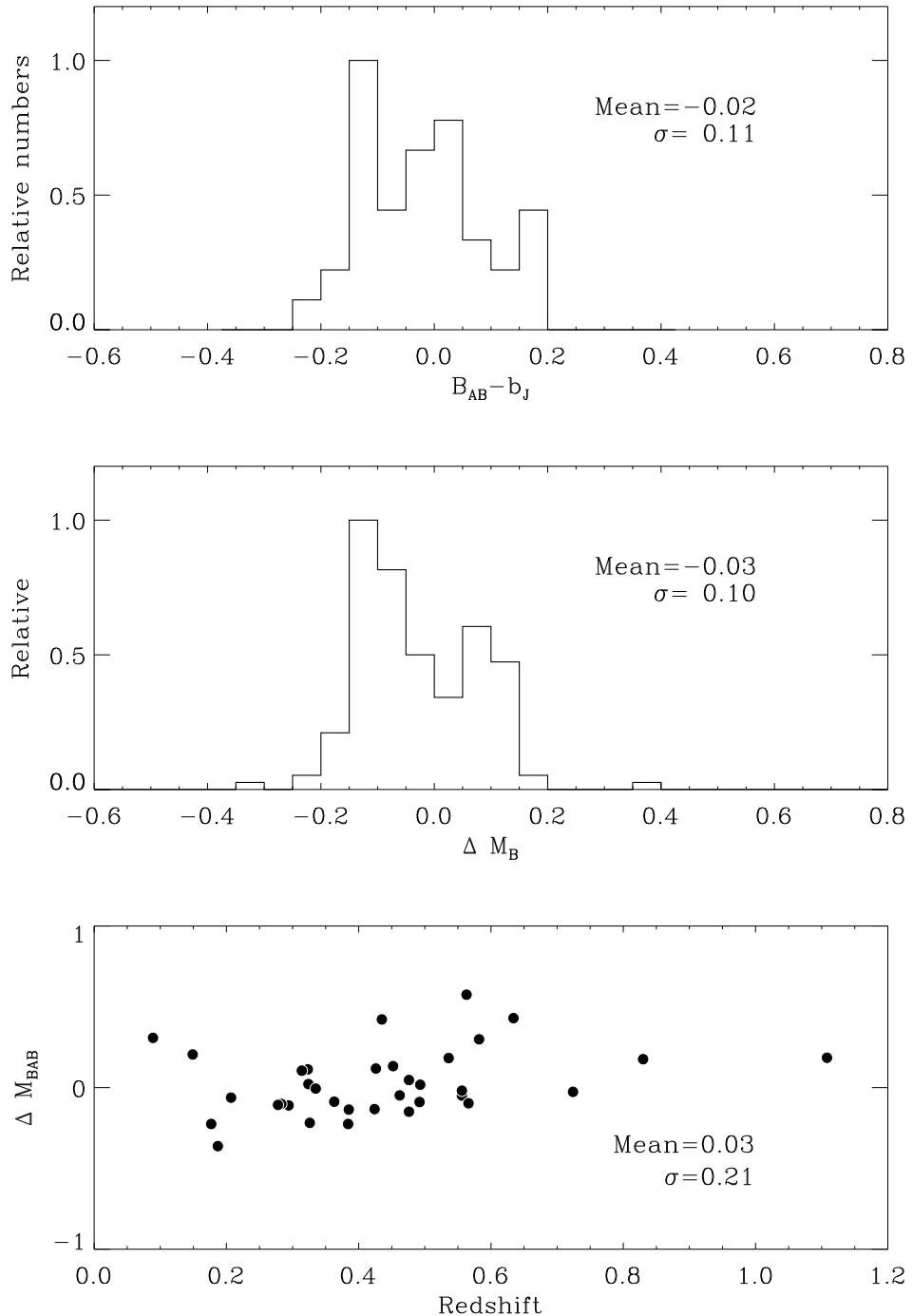
Fig. 13.— Luminosity functions as a function of *AC* class binned as in the CFRS analysis (Lilly et al. 1995b). The dotted line is the CFRS $0.2 < z < 0.5$ luminosity function.

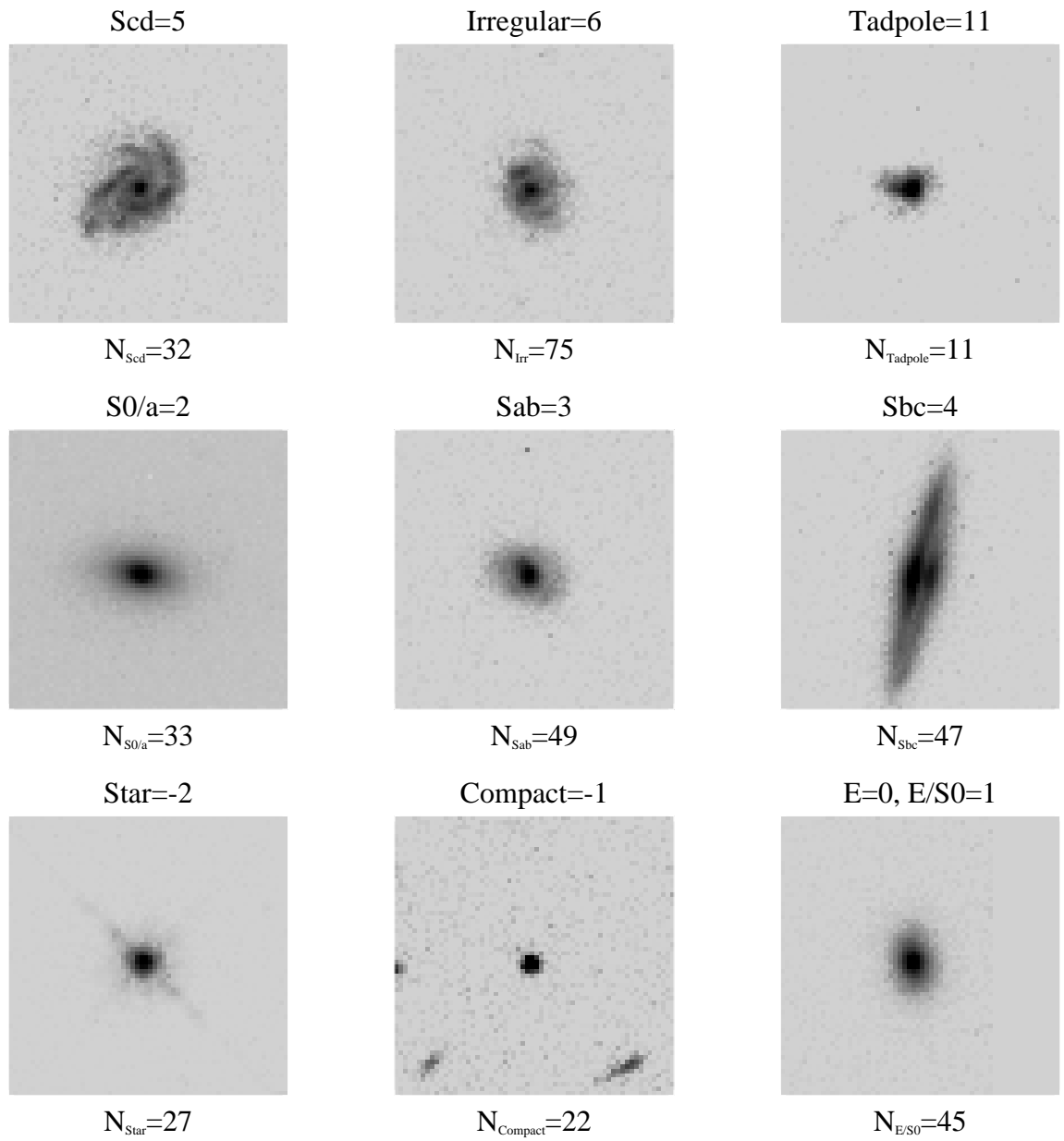
Fig. 14.— The B_{AB} rest-frame luminosity density of galaxies detected in the survey as a function of redshift and *AC* class. The values plotted are offset in redshift slightly for clarity. The downward arrow indicates the effect of a bandshifting correction of 24% for the $AC - P$ class. The open symbols represent the corrected luminosity densities, as discussed in the text.

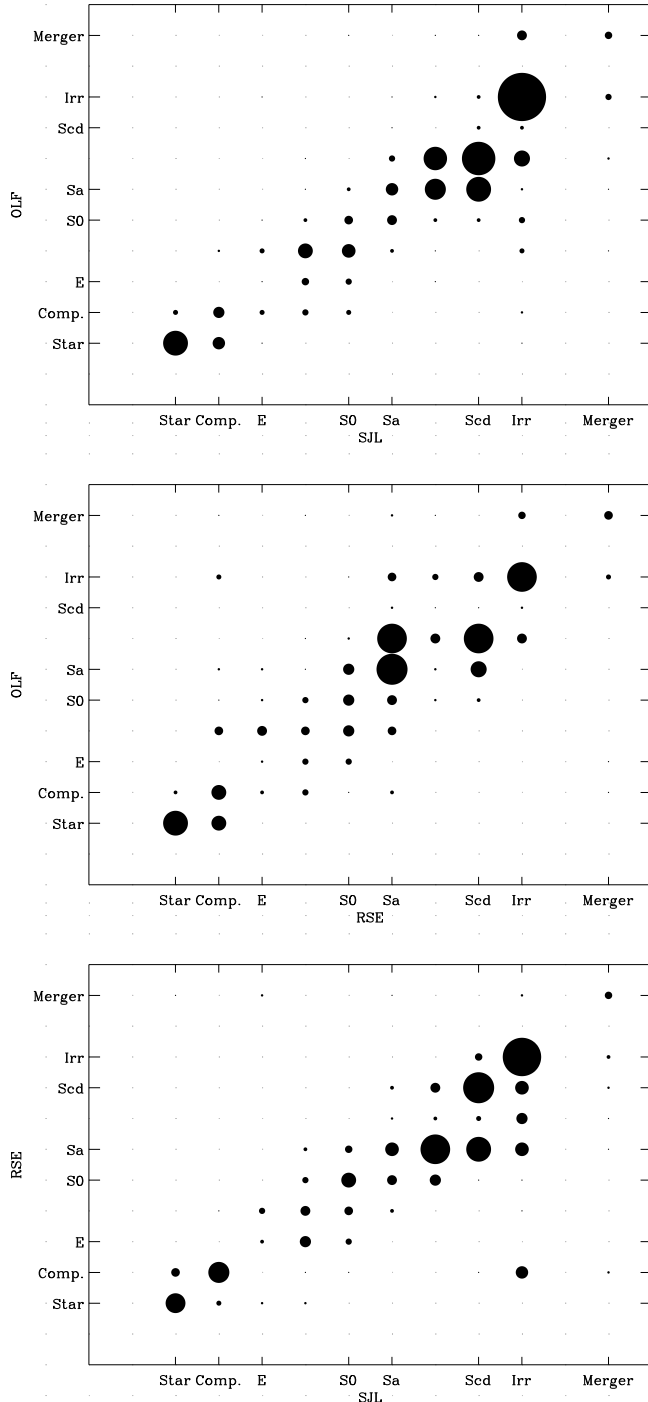
Fig. 15.— Star formation density for detected sources as a function of redshift for the three *AC* classes calculated using equation (4). The upward arrows show the total in each redshift bin. The downward arrow indicates a change of 24% in ρ_{SFR} for *AC*-peculiars

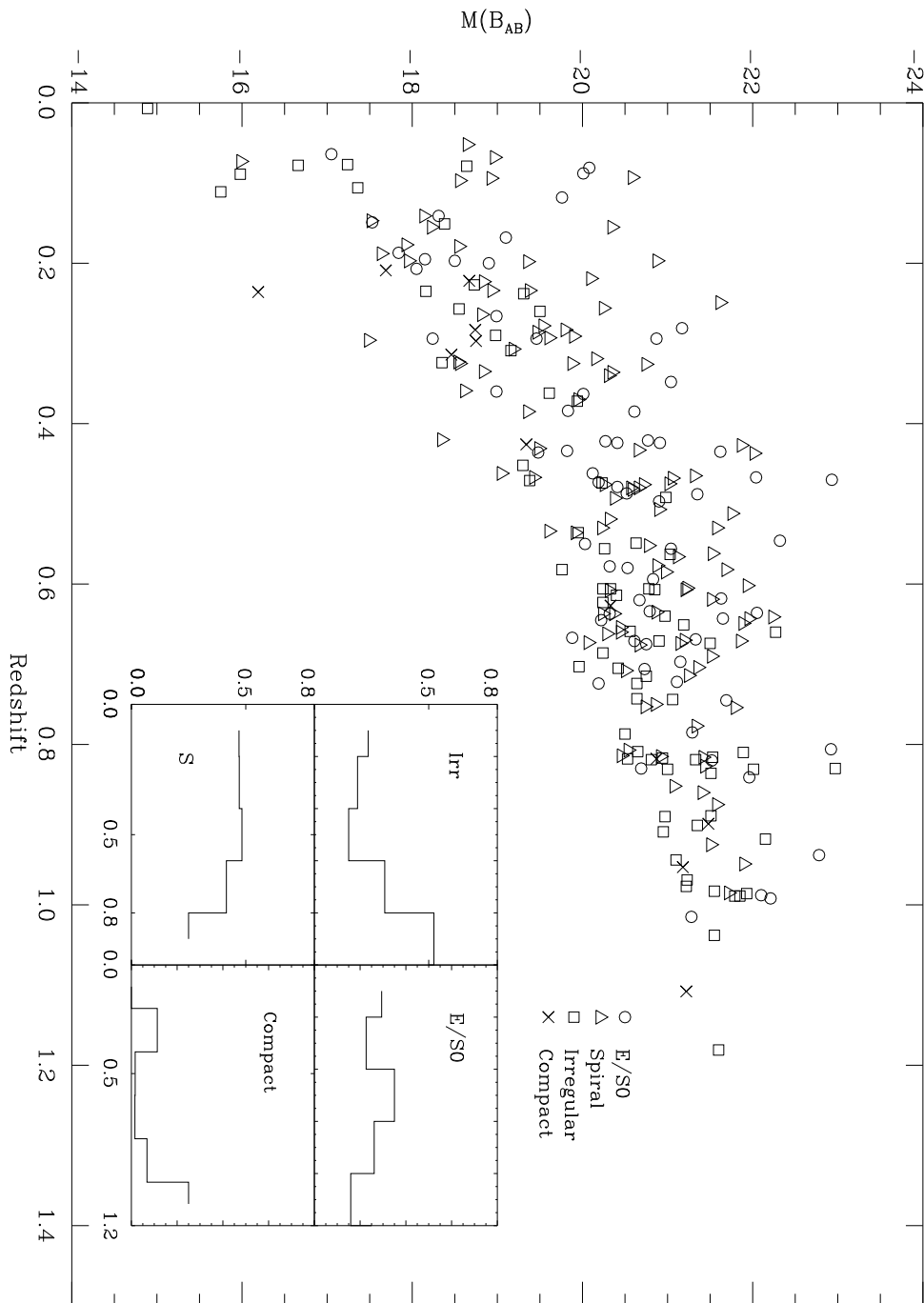


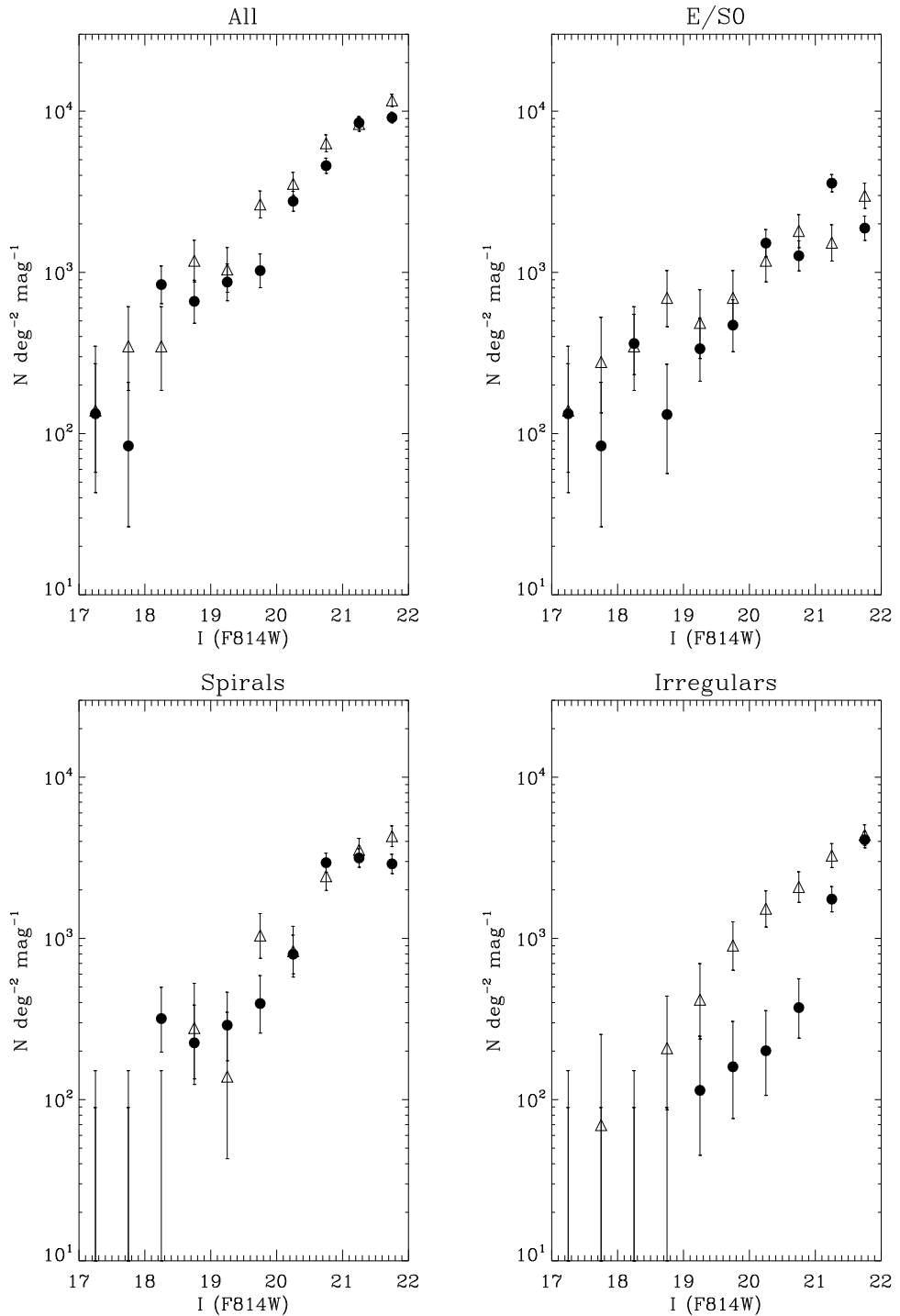


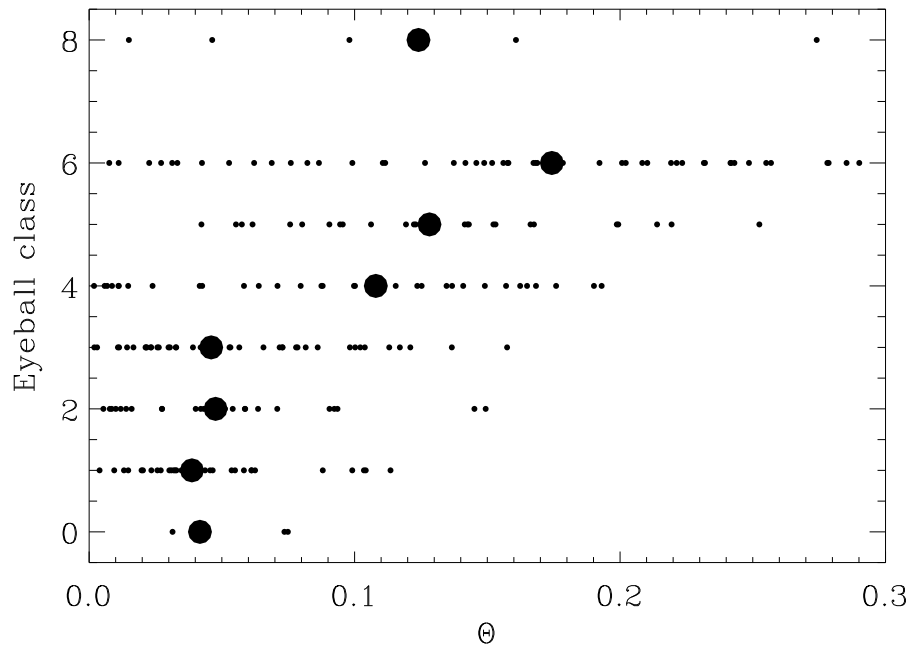
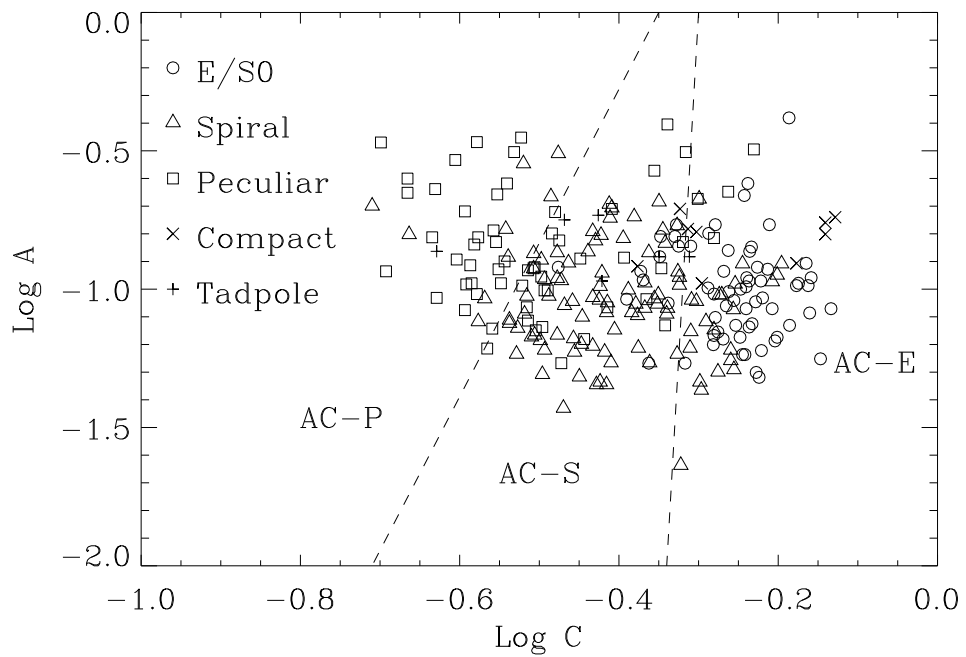


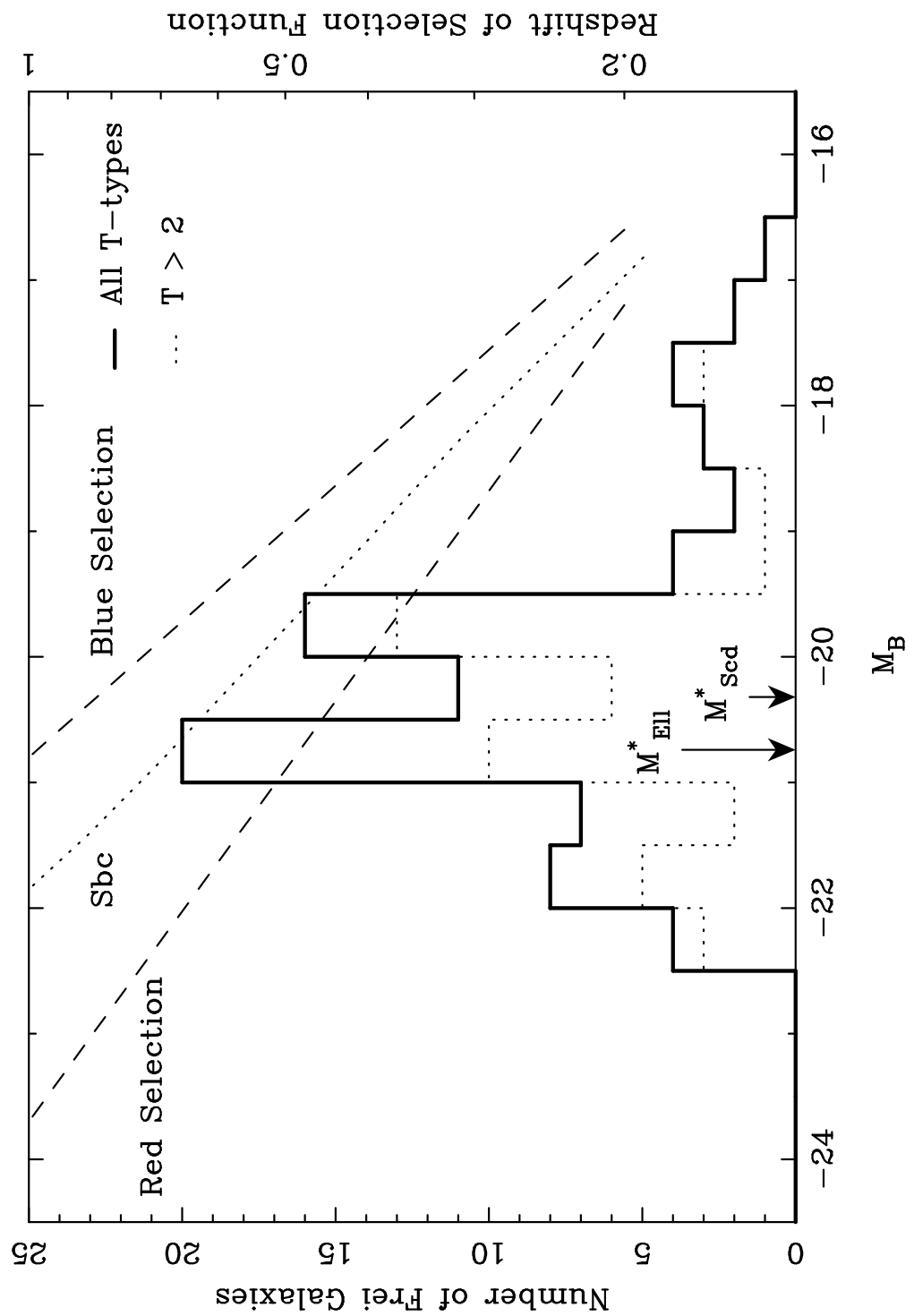


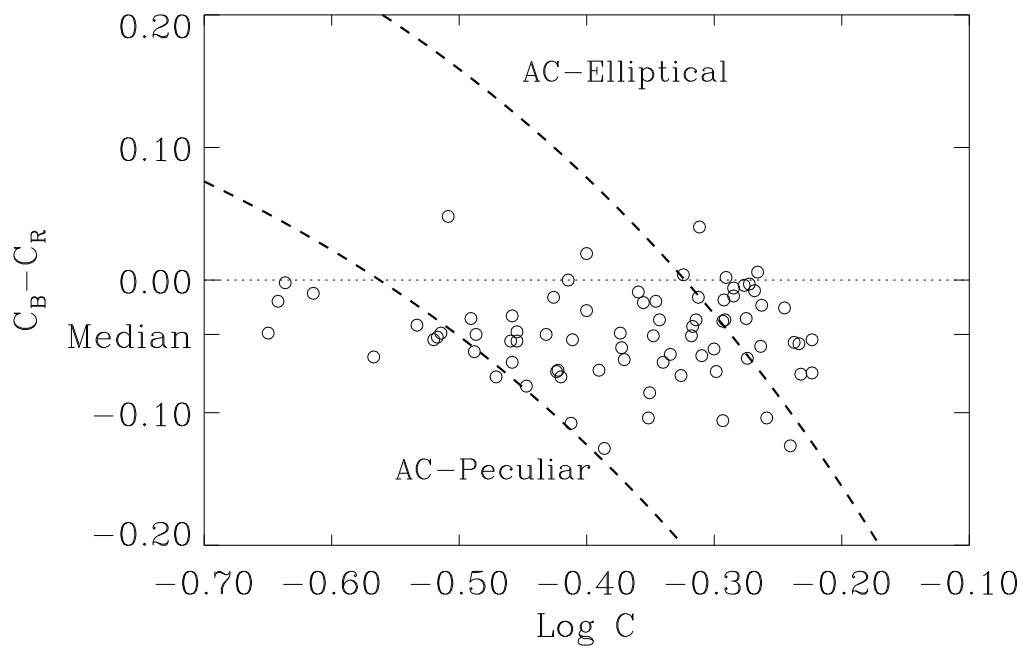
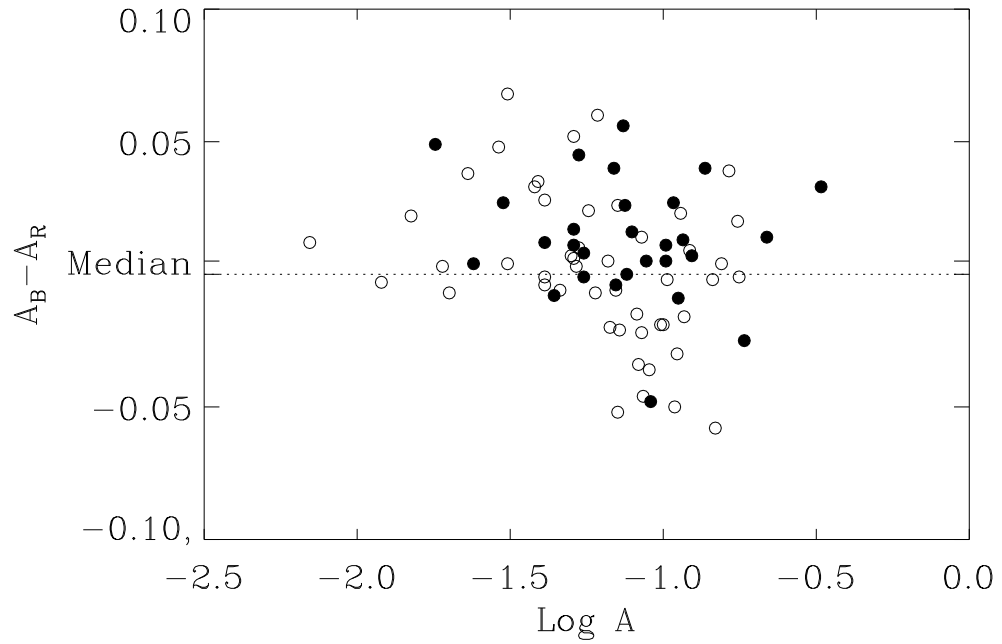


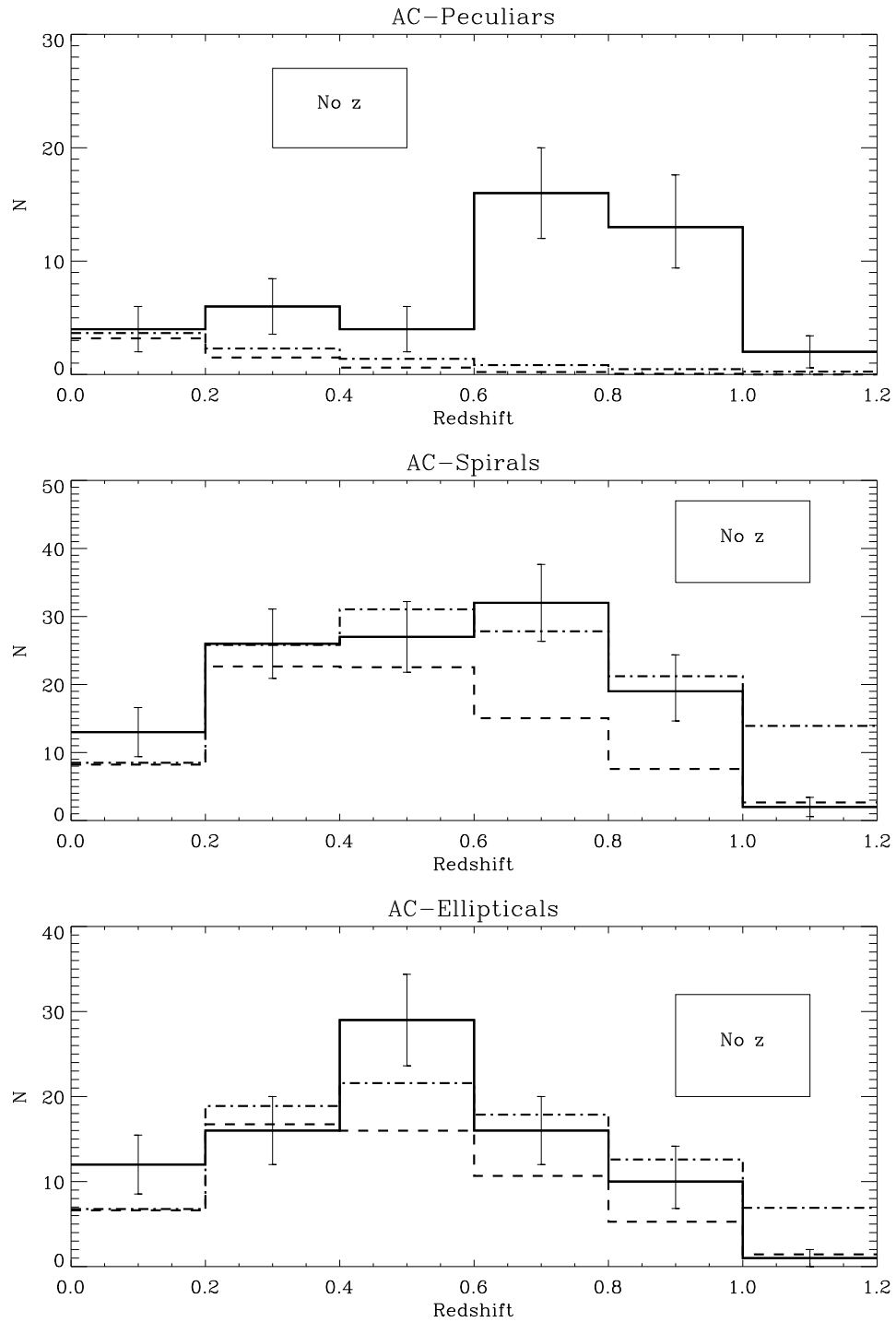


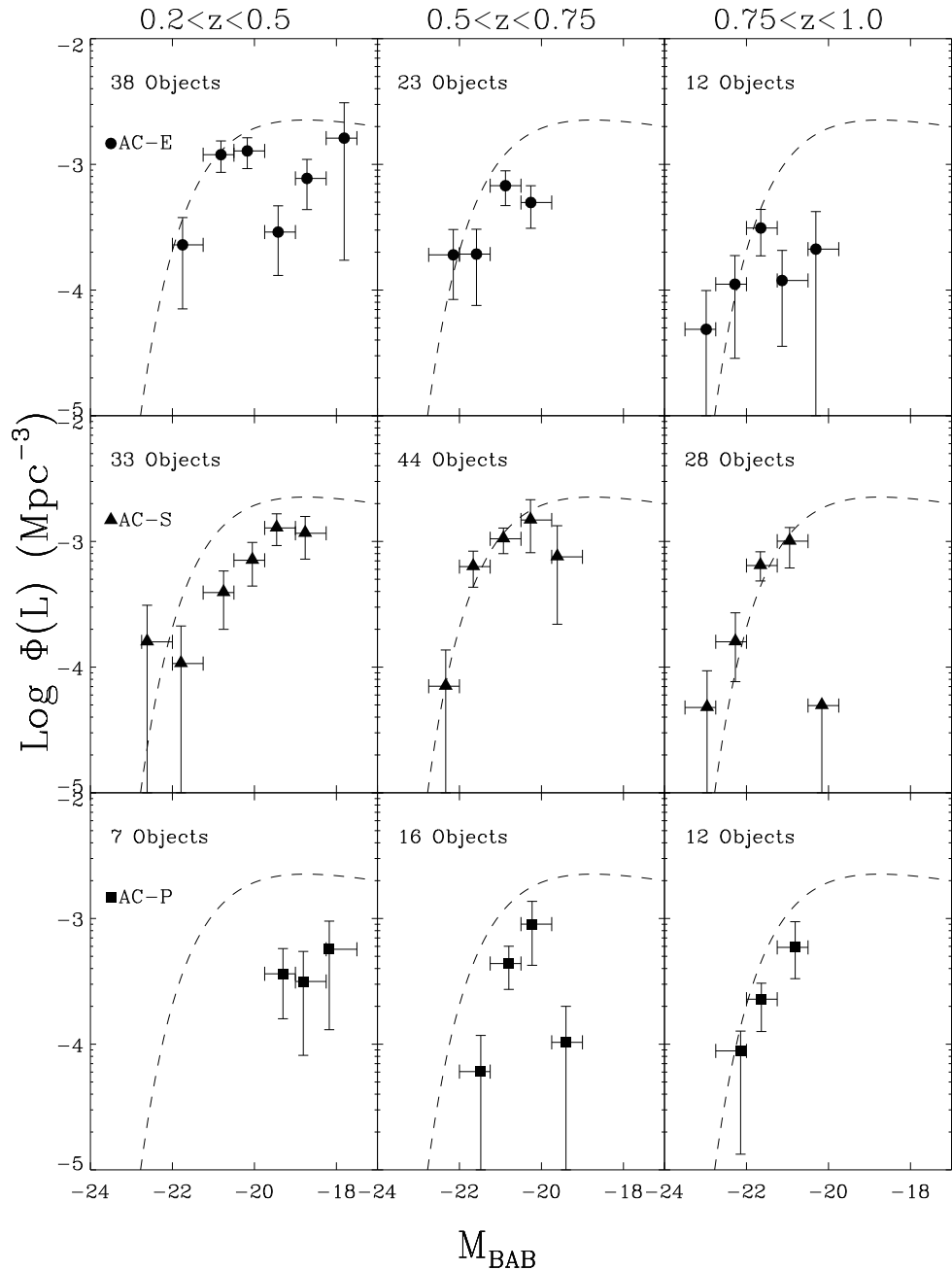


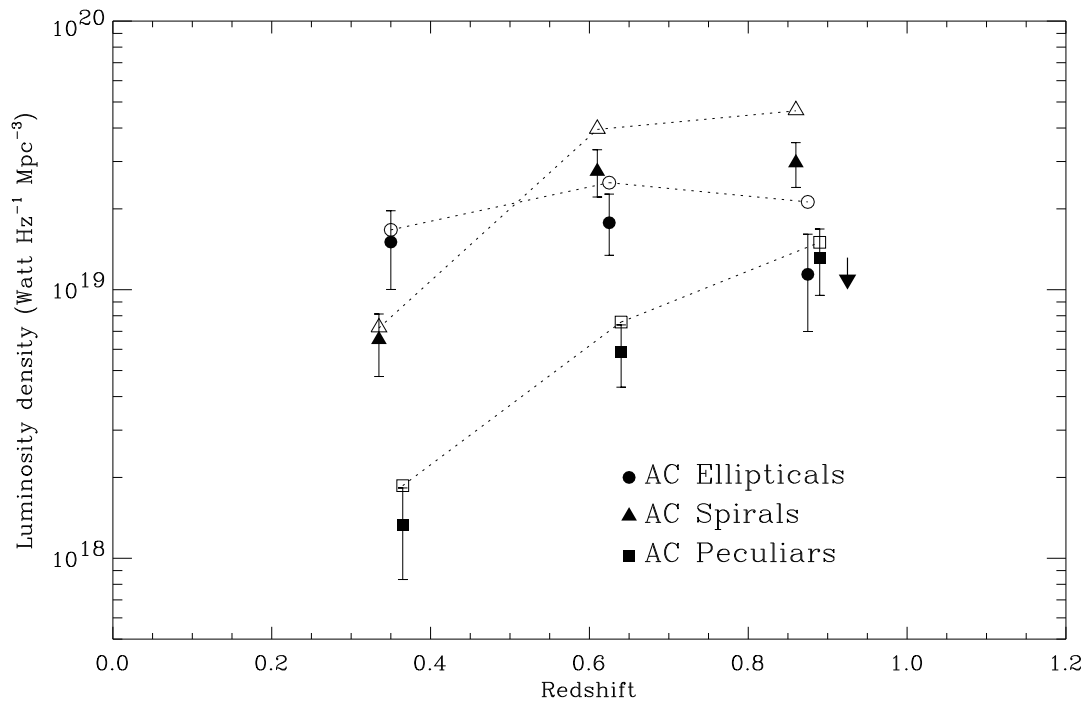


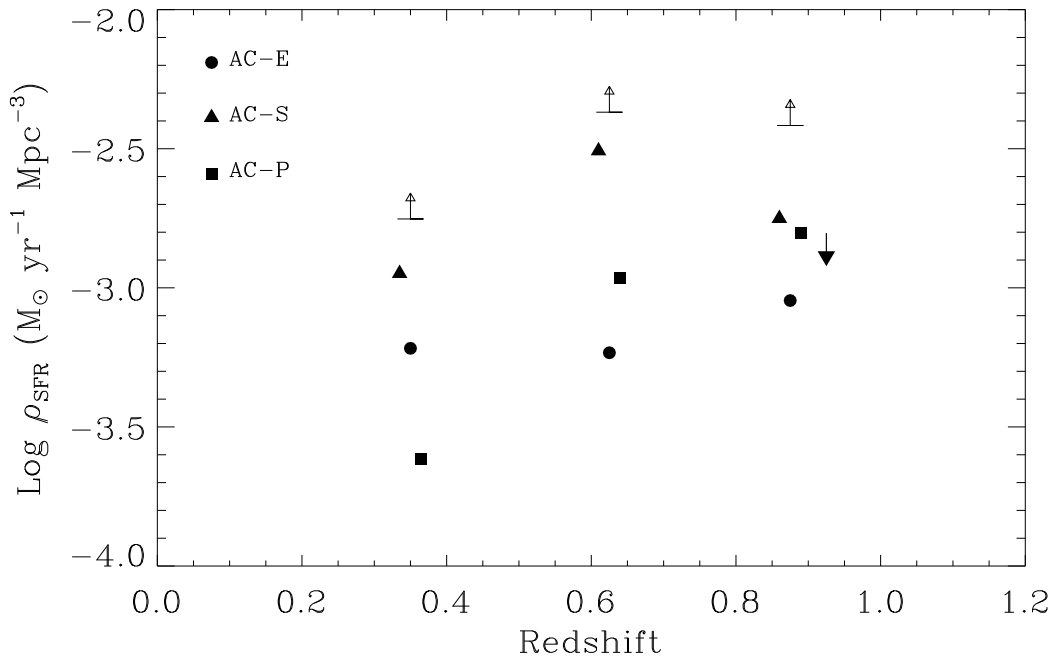












This figure "f11a.gif" is available in "gif" format from:

<http://arxiv.org/ps/astro-ph/9712060v1>

This figure "f11b.gif" is available in "gif" format from:

<http://arxiv.org/ps/astro-ph/9712060v1>

This figure "f11c.gif" is available in "gif" format from:

<http://arxiv.org/ps/astro-ph/9712060v1>